1-1-2012

Continuum Elasticity Modeling Of Nanostructure Evolution In Strained Film Epitaxy

Champika Gigiriwala Gamage
Wayne State University,

CONTINUUM ELASTICITY MODELING OF NANOSTRUCTURE EVOLUTION IN STRAINED FILM EPITAXY

by

CHAMPIKA G GAMAGE

DISSERTATION

Submitted to the Graduate School

of Wayne State University,

Detroit, Michigan

in partial fulfillment of the requirements

for the degree of

DOCTOR OF PHILOSOPHY

2012

MAJOR: PHYSICS

Approved by:

_____

Adviser Date

_____

_____

_____

_____

ACKNOWLEDGMENTS

Modeling the quantum dot formation in the language of mathematics inspired me during last six years with the help of various resources. It is my pleasure to appreciate all the people who pushed me to my limits to complete my thesis the level I expect. My research adviser, Prof. Zhi-Feng Huang is the guiding factor for all my research work and his continuous support, motivation, understanding and patience always encouraged me to go for this extend. I doubt most of the problems and confusions I confronted would not have been solved in such an elegant way without having his guidance. I would also like to acknowledge my committee members Prof. Lawes, Prof. Nadgorny and Prof. Elder (from Oakland University) for their support on my research in theoretical understanding as well as experimental sense, which led to have a successful end product. Many thanks goes to department chair, Prof. Ratna Naik & graduate adviser, Prof. Jogindra Wadehra for their support and advice in countless ways through out my graduate studies. Dr. Payson was also behind me at the very beginning of my teaching duties and his unique teaching strategies were precious for me to adapt to US teaching style. No less thanks go for Lashara Montgomery, Wynell Pitts, Delores Cowen, and Doris King for their kindness support to me over the years. Also I would like to thank the people who implemented the Sri Lankan free education system, which made the bridge to get my higher education in United States. Finally, very special thanks go to my family and friends for their love and kindness that they have given me not only during my studies but also throughout my life.

TABLE OF CONTENTS

LIST OF FIGURES

Chapter 1

Introduction

The study of semiconductor nanostructures has attracted great interest in recent years, due to their importance in a wide range of applications such as electronic, optical and optoelectronic devices, quantum computing, and information storage [1–3]. Development of modern day electronics strongly depends on the advancement of growing thin solid semiconductor films. Capability to precisely control the morphology and the micro-structure to have desired functionality of electronic devices is crucial in semiconductor device fabrication. Elasticity leads to long-range repulsive interactions between the adatoms on the surface as a result of epitaxially grown film on the substrate. Since the chemical interactions are short-range attractive and strong, there is competition between those two opposite forces. Generally, when a film is grown on a substrate, surface undulation will occur due to the growth instability [4]. This occurrence of morphological instability was first described by Asaro and Tiller [5] and Grinfeld [6], who discussed the stabilization and destabilization effects of film surface energy and the elastic energy which play a main role.

Understanding the formation of strained surface islands as a result of this film instability during epitaxy and controlling the sizes, shapes and the ordering of these islands is

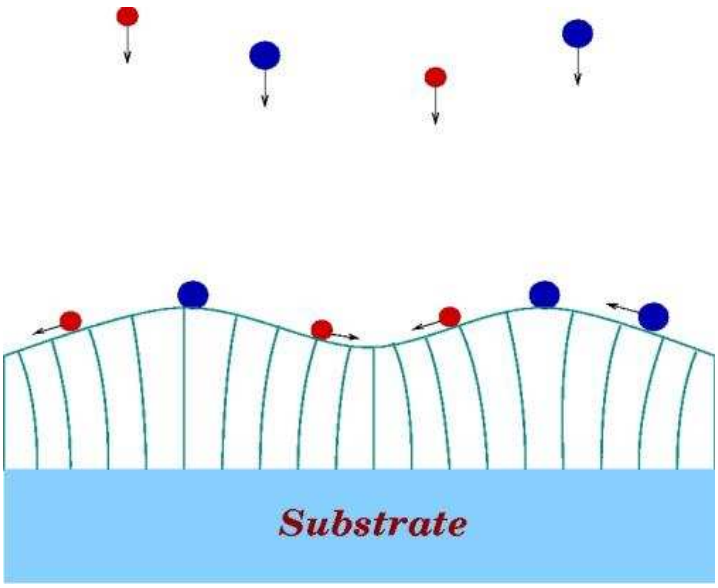

Figure 1.1. Schematic of strained film epitaxy and the formation of surface islands or quantum dots.

essential in the study of self-assembly, because,most of the electronic applications require positioning of islands at predetermined locations. Studies on how to control the formation and spatial distribution of the strained islands has become essential in the growth and fabrication of quantum dots. Many experimental and theoretical techniques have been introduced in different attempts but far more yet to be understood in the desired control of the positioning of the quantum dots for practical applications. Therefore, in this thesis work we develop a model to understand the formation and evolution of the surface nanostructures and to control the ordering of the islands by considering planar and pre-patterned substrates.

The epitaxial growth can be viewed as a process where the grown film is based on the atomic pattern of the substrate underneath as if it is the extension of the substrate structure. If a semiconductor film is grown epitaxially on a substrate, the grown material can be strained or relaxed depending on the material of the deposited crystalline structure.

There are generally two types of epitaxy: homoepitaxy and heteroepitaxy. In ho-

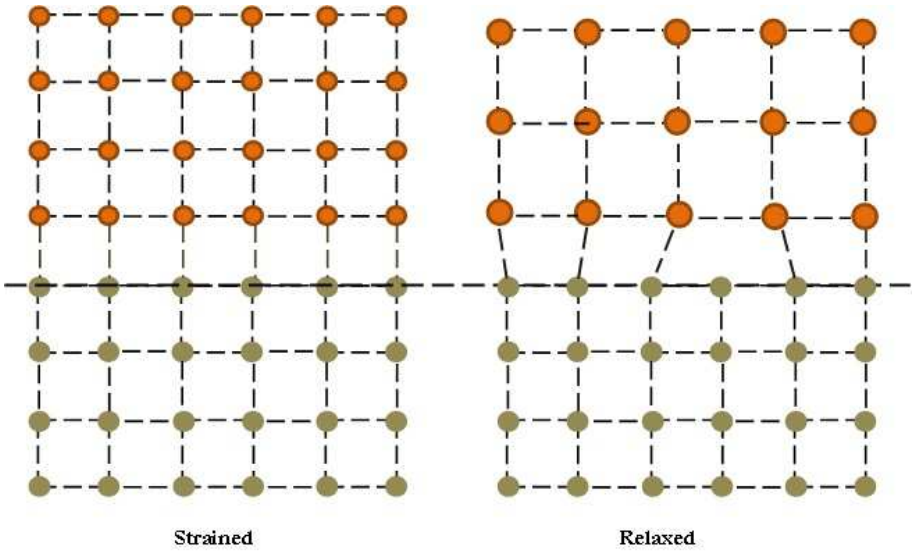

Figure 1.2. Schematic of strained film epitaxy.

moepitaxy, both the crystalline film and the substrate consist of the same material. A typical example of homoepitaxy is Si grown on a Si substrate. Main advantage in homoepitaxy is that these epitaxialy grown layers are much purer than the substrate. Heteroepitaxy is the process of growing a film crystalline on a substrate with different material that can cause strained or relaxed growth; This will lead to interfacial defects or strained surface nanostructures. Examples of such epitaxy is Ge grown on Si substrate or InAs grown on GaAs. This technology is commonly used to grow crystalline material to fabricate electronic, optical and optoelectronic devices.

Under strain (e.g. Ge on Si or InAs on GaAs with lattice mismatch), the relaxation of strain energy results in the spontaneous formation of surface structures such as small islands (quantum dots), as seen in Fig. 1.1. The difference between relaxed and strained films is clearly shown in Fig. 1.2.

Surfaces of these strained films with spontaneous undulation and roughness are usually of nanostructured configuration. Such surface undulations reduce the stress in the growing film. Various attempts have been made to explore the lateral patterning of thin

film systems in order to attain confinement in all three spatial dimensions.

The techniques that are used to grow high quality semiconductor films can be mainly classified according to the phase of the material- such as liquid phase epitaxy, vapor phase epitaxy and the molecular beam epitaxy. In liquid phase epitaxy a supersaturated solution is deposited on a substrate. Generally this technique is used to grow compound semiconductors with thin, uniform and high quality layers. Vapor Phase Epitaxy (VPE) is a technique to form a thin solid film on a substrate using a chemical vapor deposition method. This method has the main advantage of growing films of uniform distributions over a large surface areas and also drawbacks of some safety and contamination concerns. Molecular Beam Epitaxy (MBE) is a widely used technique to produce high quality semiconductor thin films in ultra high vacuum environment. The growth mechanism of MBE is not that complex and the process starts with heated sources of atomic species, which can produce clusters of atoms. These atoms then move through an ultra high vacuum environment until they reach the hot substrate surface where they need to be deposited.

1.1 Epitaxial growth modes

Epitaxial growth depends on several parameters, most importantly, on the lattice mismatch between the film and the substrate. Different types of growth modes can be found during thin film epitaxy. These growth modes also depend on the surface and interface energies, as shown in Fig.1.3.

In homoepitaxy, the difference in free energies between a single adatom at the surface and an atom incorporated in an island determines the nucleation and the growth of 2D islands. In other words, when the surface energy of the substrate is less than the total energies of the film and the interface, $\gamma_S < \gamma_{SF} + \gamma_F$ we can see 2D island formation.

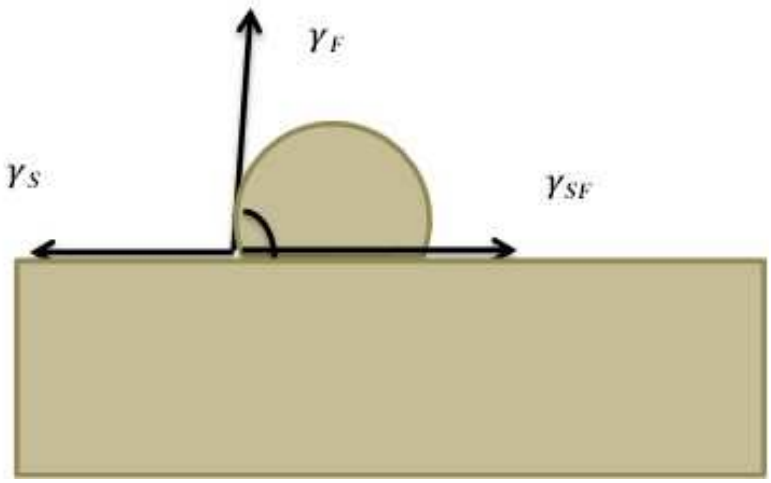

Figure 1.3. Surface energies; γ_S: surface energy of the substrate, γ_F: surface energy of film and γ_{SF}:interface energy of substrate-film

If those 2D islands coalesce, a smooth monolayer is formed. This is known as layer-by-layer growth [1, 4, 7]. In this layer-by-layer growth, the surface energy is higher than the total of the film and interface energies. The opposite of this growth mode is the three-dimensional island formation which is known as the Volmer-Weber (VW) growth. In VW growth, three dimensional islands grow due to the strong interaction between adatoms. These interactions are much stronger than the interaction between adatoms and the surface. In the Stranski-Krastanow growth mode, which is the intermediate case, the nucleation of 3D islands occurs on a smooth surface of wetting layer for large enough misfit values. In this growth method, island nucleation has to overcome a certain activation energy which depends on island volume. It has been found that under given growth conditions these islands have well defined sizes and shapes which are usually stable against ripening [1, 8–10].

In a competing strain relief mechanism, misfit dislocations are created at the film surface without roughening the wetting layer. Under certain growth conditions, e.g., at low temperature, there is a high probability for the nucleation of misfit dislocations than

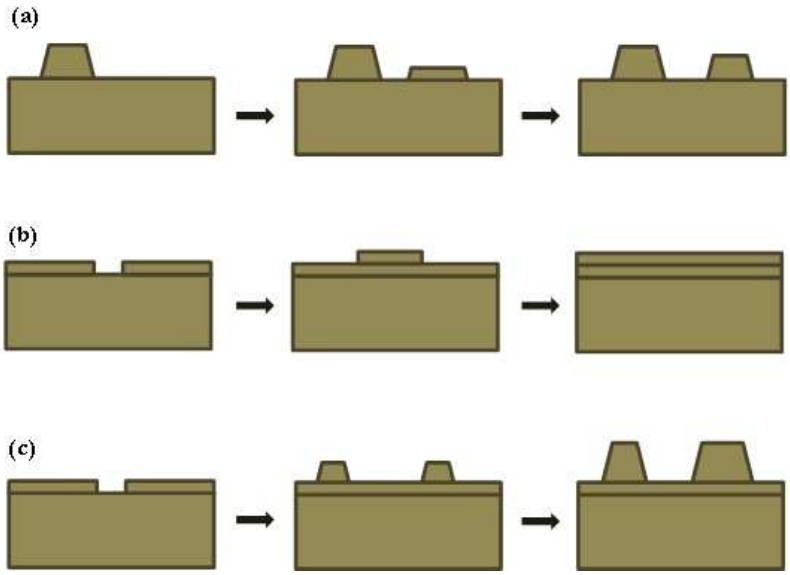

Figure 1.4. Different types of growth mode (a) Volmer-Weber growth mode (b) layer-by-layer growth mode (c) Stranski-Krastanow growth mode.

the appearance of structures formed by surface diffusion. Most of these dislocations have a tendency to create at the island-layer interface [1, 2, 11].

An important factor of the formation of quantum dots is the correlation of quantum dot positions which highly affects the nanostructured film qualities. The homogeneity of a growing island series depends on the size and shape of the semiconductor island and is affected by the periodicity of the island distribution at the growth surface. The morphology of the growing surface and the inhomogeneous surface stress are two main factors that affect the nucleation positions of islands.

1.2 Morphological instability

As we already discussed, strain builds in the presence of lattice mismatch during epitaxy. This is due to the misfit with the lattice spacing of the substrate. If the misfit strain, ϵ, greater than zero, i.e. if the equilibrium lattice spacing of the film is larger than the

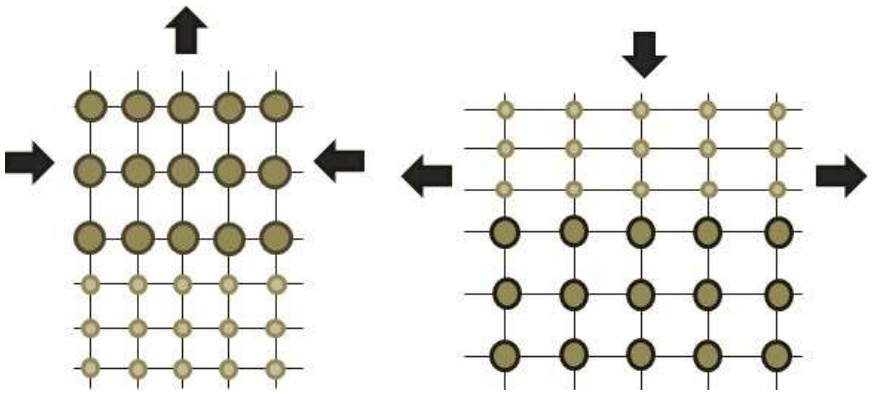

Figure 1.5. Schematic diagram of (a)compressive and (b)tensile strain

substrate, the film is compressed horizontally so the strain is compressive. On the other hand if the lattice spacing of the substrate is larger than that of the film, the strain is tensile. In our studies such as the growth of SiGe/Si we use compressive strain. Fig. 1.5 illustrates the difference between compressive and tensile strain.

In the Stranski-Krastanov growth, there are three stages of strain relief. The first stage is the growth of the wetting layer which consist of several monotonic layers. Then the so-called Asaro-Tiller-Grinfeld (ATG) instability occurs as the film becomes unstable [5]. In the final stage, strained 3D islands are formed. This reduces the strain energy while increasing the surface energy.

In order to understand the ATG instability, we consider the strain energy density, which is the product of the stress and the strain tensors. In a flat film, there is a uniform strain when a uniform uniaxial stress is applied. In the absence of surface fluctuation, the film can be in a meta-stable state. Instead of a planar film surface, if there is a perturbation on the surface as shown in Fig. 1.1, there can be nonuniform stress along the film surface. As a result, there can be stress relaxation at the peaks and stress concentration at the valleys. This relaxation of the peaks would occur because they are less constrained from the bulk. Due to this relaxation, the peaks have less strain energy than at the valleys which would lead to instability [12]. This leads to a mass transport

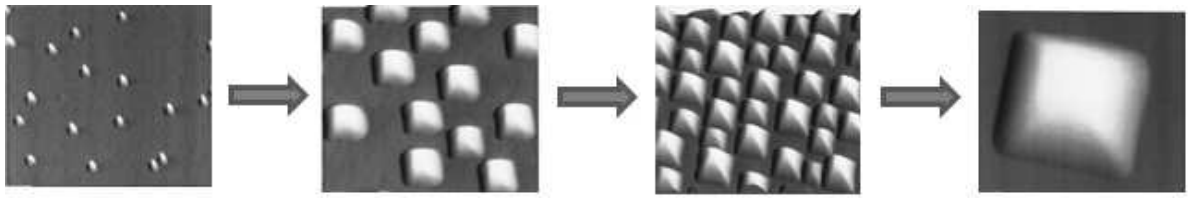

Figure 1.6. Coarsening of strained islands of Ge grown on Si [14]

from valleys where there is high strain energy to peaks with low strain energy and the peaks can be seen growing at the expense of the valleys. It causes the morphological instability of the film, and hence the formation of strained islands or quantum dots on the film surface (see Fig.1.1).

In order for the growth of islands, the mean free path of the adatoms should be smaller than the mean distance of monolayer steps [1]. By obtaining the free energy difference between adatoms on the surface and on an island, nucleation and growth of islands can be well understood. Once the island size gets larger and exceeds a critical size, coarsening process occurs: the large islands grow while the small ones disappear [1] as seen in Fig.1.6. It has been found that under given conditions, Stranski-Krastanow-grown islands have well defined sizes and shapes. There are several forms of islands; prepyramids, square pyramids, elongated pyramids and domes. The elongated pyramids or hut clusters need low growth temperature while pyramids and domes need higher temperatures for the growth [13].

1.3 Experimental results

In order to understand the formation of quantum dots or strained islands, detailed instability analysis has been studied for both single-component [15–18] and alloy strained films [19–23] as well as multilayers/ superlattices [24–27]. This instability is well observed in experiments of semiconductor heteroepitaxial films such as SiGe which shows

faceted 3D islands or unfaceted-surface morphology without nucleation [8, 18]. In these experiments, it has been seen that surface roughening and undulations first occur in dislocation-free films. During the subsequent process of island formation, the initial stage is the formation of small ripples and cell-like structures developed along the surface. Then the undulation or surface ripple amplitude grows which is followed by the creation of three dimensional islands. An example for the nonlinear evolution of the strained islands beyond the linear stability stage is the coarsening of quantum dot islands, which shows an increase of average island size during film evolution and a shrinking of small dots. This scenario with different mechanisms and behavior of coarsening has been observed in experiments of Ge/Si(001) [28,29,32,33], SiGe/Si(001) [30], and InAs/GaAs(001) [31]. Also, the slowing [28] or suppression [32] of coarsening process at late stage and the resulting saturated, stabilized quantum dot arrays [32–34] have been observed in some experiments, but not others [30].

Several studies has been carried out to find techniques to control the lateral placement of semiconductor nanostructures by e.g., reducing the surface diffusion kinetics during growth [35] and pre-patterning the substrate. Deposition of Ge on patterned Si(001) surfaces that consist of periodic arrays of Si mesas can control the self assembly of Ge islands by changing the size of the Si mesas [36]. These islands can be obtained in a "one island on one mesa" [36] relationship by minimizing the sizes of the Si mesas. When Ge islands are grown on Si substrate of stripe patterns, the formation of islands can be well seen inside the stripes of the Si substrate [37,38]. This formation of strained islands can also be controlled by changing the stripe geometry as well as the deposited layer thickness [38]. Depending on the stripe geometry, the self assembly of the Ge islands can be seen in the middle or side walls of the grooves which can be controlled by the initial growth of the film. The shape of these islands depends on the position on the Si stripes but finally converges into dome islands with increasing Ge concentration. In the growth

of InAs on pre-patterned GaAs substrates, self assembled quantum dots are seen either on the top terraces or at the side walls or at the trenches of GaAs substrates [39]. Change of island density has been observed in these experiments by changing the depth of the patterned holes; for deeper holes higher island density is observed and for shallow holes single quantum dots are formed [40]. The quantum dot density can be also controlled by changing the initial mound density on the buffer. With the increase of the density of the GaAs buffer, decrease in the quantum dot density on the film has been observed [41]. These results can be used in device applications due to the long-range ordering of the islands [37]. Thus, understanding the precise control of strained islands formation with different substrate pattern morphology is essential.

1.4 Theoretical details

Many theoretical/computational studies have been carried out in order to understand the nonlinear island evolution but it is still far from conclusive. In addition to the techniques that incorporate crystalline details, such as kinetic Monte Carlo method with elastic interaction [42,43] and phase field crystal (PFC) model and the associated amplitude equation formalism [44–50], approaches including continuum elasticity theory [51–56, 56–64] and phase field methods, [65,66] are the main efforts to understand this nonlinear island evolution. Due to the large length and time scales involved, continuum elasticity modeling is set to be the current main avenue for studying strained island coarsening. Much recent focus has been put on the derivation and simulation of nonlinear evolution equations through approximating the system elasticity and the dynamics of film morphology via perturbation methods. The limit of perfectly rigid substrate [52, 58] and the case of infinitely thick strained film [56] were the two types of system configuration addressed in early studies. Similar approximation has been applied in recent studies to heteroepitaxial

systems consisting of a strained thin film grown on an elastic substrate, as configured in most experiments. The corresponding reduced nonlinear evolution equations have been derived and simulated, based on the long-wave or small-slope approximation of film surface profile [59, 63, 64] or the assumption of small surface gradient, [62] and also the incorporation of some physical mechanisms in thin film growth such as the wetting effect between the film and the underlying substrate.

Even though there have been many studies carried out in order to understand the properties of island formation, some properties such as coarsening and saturation of quantum dots is not well understood giving inconsistent results in various studies [53, 54, 57, 61–64, 67]. In most simulations of film annealing, different coarsening rates have been found in different approaches [57,63,64] while reproducing the coarsening of strained island arrays. One main difference is the result for asymptotic and steady state of the film morphology. In the studies of reduced nonlinear evolution equation [62, 67] and in the direct solution of the full elasticity problem [53,54,61], persistence of stable quantum dot arrays after the coarsening stage have been observed, which is consistent with some Si-Ge experiments [32–34] while in some other experiments [32–34] such scenario of the suppression or cessation of island coarsening was not found in the modeling processes [57, 63]. Sub-critical bifurcation [63] has been identified as a reason for the unstableness of regular quantum dot arrays in recent studies of nonlinear analysis of the evolution equation. It has also been found that surface energy anisotropy [53,54,61,67] plays a key role in the saturation of coarsening of islands, however, such saturation processes have also been observed without the anisotropy effect [62]. These differences in the results can be due to several reasons: different approximations, different types of ways of small variable expansion and truncations involved and difficulty in using large system sizes and evolution times as needed for the comparison to experiments.

In this research, we develop a systematic approach for approximately solving the

film-substrate elastic state via a perturbation analysis in Fourier space to understand the nonlinear evolution of strained quantum dot islands grown epitaxially on an elastic substrate at large spatial and temporal scales. We consider two main approaches with planar substrate and pre-patterned substrate. In the case of planar substrate, we consider the results up to the second and third order perturbation of surface morphology. This perturbation method can be extended to obtain higher order solutions although the process is more complicated. We then derive a new dynamic equation to systematically examine the island evolution of the surface profile for large enough spatial and temporal scales. Coarsening and saturation process in post-deposited films is studied with the consideration of the wetting interaction in the nonlinear equation. It has been found in recent studies [45, 46] that films with weak strain limits can be well described using continuum elasticity theory. Therefore we study the effect of the small misfit strain that corresponds to large length scales when compared to scale of the crystalline lattice. All our results in the numerical simulation are reproducible. We found three characteristic regimes: island formation at early times, coarsening of islands at intermediate times and the saturation at later times. We also identify that the island growth and coarsening can be well described by considering the effect of higher-order elastic energy of individual islands and the elastic interaction between them. Up-to second order perturbation of surface morphology is studied for the case of pre-patterned substrates through considering the effect of the substrate pattern symmetry and wavelength and the film layer thickness. The linear analysis has been carried out to identify the wave number of film surface nanostructure with maximum instability, in particular the influence of substrate pre-pattern periodicity and amplitude as well as the effect of deposited film thickness.

Chapter 2

Quantum dot formation and evolution on planar substrate

2.1 Continuum elasticity model for strain film heteroepitaxy

As described in the previous chapter, due to the presence of elastic stress and the stress relieving procedure, epitaxially deposited films can go through transitions from layer-by-layer to the growth mode that leads to strained surface islands. Therefore to understand the stressed state of an epitaxially strained film, we use the continuum elasticity theory. Due to the diffusion process of surface atoms, the film-vapor surface moves correspondingly and evolves with time. Similarly the film-substrate interface will also move due to diffusion within the bulk phases. However, since the bulk diffusion is slower than surface diffusion, we assume that there is no inter diffusion between the film and the substrate.

Consider a strained film of a spatially varying height $h(x, y, t)$, which is deposited epitaxially on a semi-infinite elastic substrate that occupies the region $z < 0$. We assume

that the film occupies the region $0 < z < h(x, y, t)$ and the vapor occupies the region $z > h(x, y, t)$. We also assume that vapor is at zero pressure and the film and substrate are distinct crystalline solids, without dislocations or grain boundaries The film completely wets the substrate when it is deposited on the substrate and there is no misfit dislocation at the interface of the film and the substrate.

If a_f and a_s are the lattice spacing of the epitaxial film and the substrate respectively, the misfit strain in the film is given by

$$\epsilon = (a_f - a_s)/a_s. \tag{2.1}$$

If $\epsilon > 0$, i.e. if the lattice spacing of the film is larger than the substrate, the film is compressed horizontally. The evolution of the film surface morphological profile $h(x, y, t)$ for such coherent, dislocation-free system is governed by

$$\frac{\partial h}{\partial t} = \Gamma_h \sqrt{g} \nabla_s^2 \frac{\delta \mathcal{F}}{\delta h} + v, \tag{2.2}$$

where Γ_h represents the kinetic coefficient determined by surface diffusion, ∇_s^2 is the surface Laplacian, v is the deposition rate, and $g = 1 + |\nabla h|^2$ is the determinant of the surface metric. Here the effect of film-substrate inter-diffusion is neglected. In this study the total free energy functional $\mathcal{F}$ consists of two contributions

$$\mathcal{F} = \mathcal{F}_{el} + \mathcal{F}_s \tag{2.3}$$

where $\mathcal{F}_{el}$ is the elastic energy and $\mathcal{F}_s$ is the surface free energy. The elastic energy is given by

$$\mathcal{F}_{el} = \int_{-\infty}^{h} d^3 r \mathcal{E} \tag{2.4}$$

where $\mathcal{E}$ represents the strain energy density, and the surface free energy is represented by

$$\mathcal{F}_s = \int d^2 r \gamma(h) \sqrt{g} \tag{2.5}$$

where γ is the thickness-dependent, isotropic surface tension which include the effect of wetting interactions between the film and substrate. With these free energies, the dynamical equation (2.2) then becomes [17, 59, 63]

$$\frac{\partial h}{\partial t} = \Gamma_h \sqrt{g} \nabla_s^2 \left[\gamma \kappa + W(h) + \mathcal{E}^f \right] + v, \tag{2.6}$$

where κ is the mean surface curvature, $\mathcal{E}^f$ gives the film elastic energy density at the surface $z = h$, and W is the wetting potential [63] that depends on the film thickness:

$$W(h) = -w \left(\frac{h}{h_{ml}} \right)^{-\alpha_w} e^{-h/h_{ml}}. \tag{2.7}$$

Here w gives the strength of the film-substrate wetting interaction, h_{ml} is the characteristic wetting-layer thickness that is usually of few monolayers, and the exponent α_w (> 0) gives the singularity of the potential W in the limit of $h \to 0$ that emulates the persistence of the wetting layer during film evolution [63].

The elastic energy density in isotropic, linear elasticity theory is given by

$$\mathcal{E} = \frac{1}{2} \sigma_{ij} u_{ij} \tag{2.8}$$

where $i, j = x, y, z$, and u_{ij} is the linear elastic strain tensor defined by

$$u_{ij} = (\partial_j u_i + \partial_i u_j)/2 \tag{2.9}$$

with u_i being the ith Cartesian component of the displacement field with index $i = 1, 2, 3$

corresponding to the x, y, z components respectively. In the above expression the term ∂_i indicates the partial derivative with respect to the ith coordinate. The stress tensor σ_{ij}^f in strained film for an isotropic elastic system is given by the Hooke's law as

$$\sigma_{ij}^f = 2\mu \left[\frac{\nu}{1-2\nu} \delta_{ij} u_{kk}^f + u_{ij}^f - \frac{1+\nu}{1-2\nu} \epsilon \delta_{ij} \right], \tag{2.10}$$

and the stress tensor σ_{ij}^s in the substrate is given by

$$\sigma_{ij}^s = 2\mu \left[\frac{\nu}{1-2\nu} \delta_{ij} u_{kk}^s + u_{ij}^s \right], \tag{2.11}$$

where μ is the shear modulus, ν is the Poisson ratio and the subscripts "f" and "s" refer to the film and substrate phases, respectively. The stress tensor in the substrate is also given by Eq. (2.10) with $\epsilon = 0$. In our analysis we assume equal elastic constants in the film and substrate because in most experiments their difference is not significant.It is assumed that the mechanical equilibrium condition $\partial_j \sigma_{ij} = 0$ exists in both the film and the substrate because the elastic relaxation occurs on a time scale of orders of magnitude faster than that of the atomic diffusion process and the associated system morphological evolution. By substituting Eq. (2.10) to the mechanical equilibrium equation, we obtain Navier's equations in the whole film-substrate system as

$$(1-2\nu)\partial_j^2 u_i + \partial_i \partial_j u_j = 0, \tag{2.12}$$

which can be applied to both the film and the substrate.

Due to the negligible external pressure on the free surface, we have the corresponding boundary condition on the top film surface as

$$\sigma_{ij}^f n_j = 0 \qquad \text{at } z = h(x, y, t). \tag{2.13}$$

Here n_j is the unit normal to the film surface. This normal vector is oriented toward the vapor. The continuity of the displacement in the film-substrate interface gives

$$u_i^f = u_i^s \qquad \text{at } z = 0, \tag{2.14}$$

and the continuity of the stress leads to

$$\sigma_{ij}^f n_j = \sigma_{ij}^s n_j \quad \text{at} z = 0, \tag{2.15}$$

where n_j is the unit vector normal to the interface, showing the coherency at the film-substrate interface.

Finally, inside the substrate region that is far away from the film we have

$$u_i^s, u_{ij}^s \to 0 \qquad \text{for } z \to -\infty. \tag{2.16}$$

The above equations are defined for a given configuration of the free surface $z = h(x, y, t)$.

2.2 Perturbation analysis and nonlinear evolution equation

In order to solve this elasticity problem, we apply perturbation analysis in Fourier space. We perturb the basic solution to small vertical variation of film surface profile. The Fourier transform of the film morphological profile can be written as

$$h = \bar{h} + \sum_q \hat{h}(\mathbf{q}, t) e^{i(q_x x + q_y y)}, \tag{2.17}$$

where $\bar{h} = h_0 + vt$ is the average film thickness at any time t and h_0 the initial film thickness. It is also possible to expand the Fourier components of the displacement field $\hat{u}_i(\mathbf{q})$, stress tensor $\hat{\sigma}_{ij}(\mathbf{q})$ $(i, j = x, y, z)$, and film elastic energy density $\hat{\mathcal{E}}^f$ in the order of surface perturbation $\hat{h}(\mathbf{q})$. The corresponding expansions are written as

$$u_i = \bar{u}_i + \textstyle\sum_q \hat{u}_i(\mathbf{q}) e^{i(q_x x + q_y y)}, \qquad \sigma_{ij} = \bar{\sigma}_{ij} + \textstyle\sum_q \hat{\sigma}_{ij}(\mathbf{q}) e^{i(q_x x + q_y y)},$$
$$\mathcal{E}^f = \bar{\mathcal{E}}^f + \textstyle\sum_q \hat{\mathcal{E}}^f(\mathbf{q}) e^{i(q_x x + q_y y)},$$

with

$$\hat{u}_i = \hat{u}_i^{(1)} + \hat{u}_i^{(2)} + \hat{u}_i^{(3)} + \cdots, \qquad \hat{\sigma}_{ij} = \hat{\sigma}_{ij}^{(1)} + \hat{\sigma}_{ij}^{(2)} + \hat{\sigma}_{ij}^{(3)} + \cdots,$$
$$\hat{\mathcal{E}}^f = \hat{\mathcal{E}}^{(1)f} + \hat{\mathcal{E}}^{(2)f} + \hat{\mathcal{E}}^{(3)f} + \cdots. \tag{2.18}$$

For a completely relaxed substrate the base state is referred to as

$$\bar{u}_i^s = \bar{u}_{ij}^s = \bar{\sigma}_{ij}^s = 0 \qquad \text{for } i = x, y, z. \tag{2.19}$$

The reference state is chosen such that the strain coincide with the substrate lattice. Therefore the displacement and the strain in the x and y directions are 0,

$$\bar{u}_i^f = 0 \qquad \bar{u}_{ij} = 0 \qquad \text{for } i = x, y. \tag{2.20}$$

The strain u_{zz}^f is a constant as the z component of the displacement in the film is linear in the z direction. Thus the displacement and the strain in the z direction is written as

$$\bar{u}_z^f = \bar{u}_{zz}^f z, \text{ where } \bar{u}_{zz}^f = \epsilon(1+\nu)/(1-\nu) \text{ and } \bar{\sigma}_{xx}^f = \bar{\sigma}_{yy}^f = -2\mu\bar{u}_{zz}^f. \tag{2.21}$$

All the other stress tensors $\bar{\sigma}^f_{ij} = 0$ and the strain tensor can be written as $\bar{u}^f_{ij} = 0$ except for $\bar{u}^f_{zz} = \epsilon(1+\nu)/(1-\nu)$.

To the first order of perturbed quantities, the linearized boundary conditions are given by

$$\begin{aligned} \hat{\sigma}^f_{jz} &= iq_j\bar{\sigma}\hat{h} \qquad \text{where} j = x, y \\ \hat{\sigma}^f_{zz} &= 0. \end{aligned} \tag{2.22}$$

At the interface$z = 0$, the conditions due to Eqs. (2.14) and (2.15) are expanded to the first order

$$\hat{u}^f_j = \hat{u}^s_j \tag{2.23}$$

$$\hat{\sigma}^f_{jz} = \hat{\sigma}^s_{jz}, \qquad \text{for} j = x, y, z. \tag{2.24}$$

This work has been well studied previously as applied to the initial stage of the film evolution [16–18].

With the use of the linearized boundary conditions, the unperturbed (0th-order) elastic energy density can be calculated as $\bar{\mathcal{E}}^f = E\epsilon^2/(1-\nu)$ (E is the Young's modulus) and the 1st order perturbed elastic energy density as

$$\hat{\mathcal{E}}^{(1)f} = -\frac{2E(1+\nu)}{1-\nu}\epsilon^2 q\hat{h}(\mathbf{q}). \tag{2.25}$$

To obtain the elastic properties at higher orders we substitute the expansions (2.17) and (2.18) into Eqs. (2.12)–(2.16). Then the Navier's equations (2.12) in the Fourier

space can be rewritten as

$$(1-2\nu)(\partial_z^2-q^2)\hat{u}_j^{(\xi)}+iq_j\left[iq_x\hat{u}_x^{(\xi)}+iq_y\hat{u}_y^{(\xi)}+\partial_z\hat{u}_z^{(\xi)}\right]=0, \qquad \text{for } j=x,y, \tag{2.26}$$

$$(1-2\nu)(\partial_z^2-q^2)\hat{u}_z^{(\xi)}+\partial_z\left[iq_x\hat{u}_x^{(\xi)}+iq_y\hat{u}_y^{(\xi)}+\partial_z\hat{u}_z^{(\xi)}\right]=0, \tag{2.27}$$

for ξth order expansion ($\xi=1,2,3,...$). After using the boundary conditions (2.14),(2.15) and (2.16) at the film-substrate interface and inside the substrate, the corresponding general solutions for the 1st and 2nd order equations have the same format, which read

$$\begin{aligned}\hat{u}_i^{(\xi)f} &= \begin{bmatrix}\alpha_x^{(\xi)}\\ \alpha_y^{(\xi)}\\ \alpha_z^{(\xi)}\end{bmatrix}\cosh(qz)+\begin{bmatrix}\beta_x^{(\xi)}\\ \beta_y^{(\xi)}\\ \beta_z^{(\xi)}\end{bmatrix}\sinh(qz)-\begin{bmatrix}C^{(\xi)}iq_x/q\\ C^{(\xi)}iq_y/q\\ D^{(\xi)}\end{bmatrix}z\sinh(qz)\\ &-\begin{bmatrix}D^{(\xi)}iq_x/q\\ D^{(\xi)}iq_y/q\\ C^{(\xi)}\end{bmatrix}z\cosh(qz)\end{aligned} \tag{2.28}$$

for the film, and

$$\hat{u}_i^{(\xi)s}=\begin{bmatrix}\alpha_x^{(\xi)}\\ \alpha_y^{(\xi)}\\ \alpha_z^{(\xi)}\end{bmatrix}e^{qz}-\begin{bmatrix}iq_x/q\\ iq_y/q\\ 1\end{bmatrix}B^{(\xi)}ze^{qz} \tag{2.29}$$

for the substrate. The coefficients $\alpha_i^{(\xi)}$, $\beta_i^{(\xi)}$, $C^{(\xi)}$, $D^{(\xi)}$, and $B^{(\xi)}$ in Eqs. (2.28) and (2.29) are determined via the expansion of boundary conditions (2.13)–(2.15) in orders of perturbation $\hat{h}$.

For the 2nd order expansion of the boundary conditions by retaining up to 2nd order perturbed quantities, we obtain that at the top surface of the film, $z=h$, Eq. (2.13)

gives

$$-\sum_{\mathbf{q}'} i(q_x - q'_x)\hat{\sigma}^{(1)f}_{jx}(\mathbf{q}')\hat{h}(\mathbf{q}-\mathbf{q}') - \sum_{\mathbf{q}'} i(q_y - q'_y)\hat{\sigma}^{(1)f}_{jy}(\mathbf{q}')\hat{h}(\mathbf{q}-\mathbf{q}') + \hat{\sigma}^{(2)f}_{jz}(\mathbf{q}) = 0, \quad (2.30)$$

while the continuity of stress at the film-substrate interface $z = 0$ (i.e., Eqs. (2.14) & (2.15)) yields

$$\hat{\sigma}^{(2)f}_{jz}(\mathbf{q}) = \hat{\sigma}^{(2)s}_{jz}(\mathbf{q}), \quad (2.31)$$

with $j = x, y, z$. Here the subscription (1) corresponds to the 1st order perturbation terms that have been known in the linear analysis [17, 19], and (2) corresponds to the new 2nd order perturbation terms.

Substituting Eqs. (2.28) and (2.29) to these boundary conditions (2.30) and (2.31), the second order coefficients of the solution can be obtained as follows:

$$q\alpha^{(2)}_z = q\beta^{(2)}_z = -e^{-q\bar{h}}\left[\frac{a^{(2)}_1 q_x + b^{(2)}_1 q_y}{2\mu q}(1 - 2\nu + q\bar{h}) - \frac{c^{(2)}_1}{2\mu}(2 - 2\nu + q\bar{h})\right], \quad (2.32)$$

$$iq_x\alpha^{(2)}_x + iq_y\alpha^{(2)}_y = iq_x\beta^{(2)}_x + iq_y\beta^{(2)}_y = e^{-q\bar{h}}\left[\frac{a^{(2)}_1 q_x + b^{(2)}_1 q_y}{2\mu q}(q\bar{h} - 2 + 2\nu) + \frac{c^{(2)}_1}{2\mu}(1 - 2\nu + q\bar{h})\right], \quad (2.33)$$

$$C^{(2)} = D^{(2)} = B^{(2)} = e^{-q\bar{h}}\left[-\frac{a^{(2)}_1 q_x + b^{(2)}_1 q_y}{2\mu q} + \frac{c^{(2)}_1}{2\mu}\right], \quad (2.34)$$

where

$$a_1^{(2)}q_x + b_1^{(2)}q_y = \sum_{\mathbf{q}'} \hat{h}(\mathbf{q}-\mathbf{q}')\hat{h}(\mathbf{q}') \left\{ \frac{2E\epsilon}{q'(1-\nu)} \left[q_x(q_x - q'_x)(q'^2_x + \nu q'^2_y) \right.\right.$$
$$\left.\left. + q_y(q_y - q'_y)(q'^2_y + \nu q'^2_x) \right] + 2E\epsilon \frac{q'_x q'_y}{q'} \left[q_x(q_y - q'_y) + q_y(q_x - q'_x) \right] \right\} \quad (2.35)$$

and

$$c_1^{(2)} = \sum_{\mathbf{q}'} \hat{h}(\mathbf{q}-\mathbf{q}')\hat{h}(\mathbf{q}') \frac{E\epsilon}{1-\nu} \left[q'_x(q_x - q'_x) + q'_y(q_y - q'_y) \right]. \quad (2.36)$$

Based on the above solution, we can derive the second order elastic energy density, i.e.,

$$\hat{\mathcal{E}}^{(2)f} = \sum_{\mathbf{q}'} \left[\frac{1+\nu}{2E} \hat{\sigma}_{ij}^{(1)f}(\mathbf{q}') \hat{\sigma}_{ij}^{(1)f}(\mathbf{q}-\mathbf{q}') - \frac{\nu}{2E} \hat{\sigma}_{ll}^{(1)f}(\mathbf{q}) \hat{\sigma}_{ll}^{(1)f}(\mathbf{q}-\mathbf{q}') \right]$$
$$+ \frac{E\epsilon}{1-\nu} \left[(1-\nu) \frac{a_1^{(2)}q_x + b_1^{(2)}q_y}{\mu q} - (1-2\nu) \frac{c_1^{(2)}}{2\mu} \right], \quad (2.37)$$

where the expressions of 1st-order stress tensor $\hat{\sigma}_{ij}^{(1)f}$ at the top surface are given in the appendix [see Eqs. (11)–(16)]. The 2nd-order stress tensor are also shown in Eqs. (5)–(10) of the appendix.

For a composition independent surface, the dynamical equation for the nonlinear evolution of the film surface morphology [Eq. (2.6)] is derived by using the results of

perturbed elastic energy density given in Eqs. (4.6) and (2.37),

$$\begin{aligned}\frac{\partial\hat{h}}{\partial t} &= (-\gamma\Gamma_h q^4 + 2E\Gamma_h\frac{(1+\nu)}{(1-\nu)}\epsilon^2 q^3)\hat{h} \\ &-\Gamma_h\sum_{\mathbf{q}'}\left\{\frac{E(1+\nu)}{2(1-\nu)^2}\epsilon^2\frac{q^2}{q'|\mathbf{q}-\mathbf{q}'|}\left[[2(1-\nu)\left[q'_x(q_x-q'_x)\right.\right.\right. \\ &\left.\left.\left.+q'_y(q_y-q'_y)\right]-\frac{q'|\mathbf{q}-\mathbf{q}'|}{2(1-\nu)}\right]^2+\frac{16\nu(1-\nu)^3-1}{4(1-\nu)^2}q'^2|\mathbf{q}-\mathbf{q}'|^2\right] \\ &+4E\frac{(1+\nu)}{(1-\nu)}\epsilon^2\frac{q}{q'}\left[q_x(q_x-q'_x)(q'^2_x+\nu q'^2_y)+q_y(q_y-q'_y)(q'^2_y+\nu q'^2_x)\right. \\ &\left.+(1-\nu)q'_xq'_y\left[q_x(q_y-q'_y)+q_y(q_x-q'_x)\right]\right] \\ &-\frac{E(1-2\nu)(1+\nu)\epsilon^2}{(1-\nu)^2}q^2\left[q'_x(q_x-q'_x)+q'_y(q_y-q'_y)\right]\Bigg\}\hat{h}(\mathbf{q}')\hat{h}(\mathbf{q}-\mathbf{q}'). \quad (2.38)\end{aligned}$$

In order to simplify the calculation, we choose a length scale $l = \gamma/\mathcal{E}_0$ and a time scale $\tau = l^4/\gamma\Gamma_h$, where the characteristic strain energy density $\mathcal{E}_0 = 2E\epsilon_0^2(1+\nu)/(1-\nu)$ with ϵ_0 a reference misfit value. The corresponding 2nd order strain energy density then becomes,

$$\begin{aligned}\hat{\mathcal{E}}^{(2)f} &= -\epsilon^2\left[(1-\nu)\frac{[\mathbf{q}'\cdot(\mathbf{q}-\mathbf{q}')]^2}{q'|\mathbf{q}-\mathbf{q}'|}-\mathbf{q}'\cdot(\mathbf{q}-\mathbf{q}')+\nu q'|\mathbf{q}-\mathbf{q}'|\right] \\ &-\frac{2\epsilon^2}{qq'}\left\{q_x(q_x-q'_x)(q'^2_x+\nu q'^2_y)+q_y(q_y-q'_y)(q'^2_y+\nu q'^2_x)\right. \\ &\left.+(1-\nu)q'_xq'_y\left[q_x(q_y-q'_y)+q_y(q_x-q'_x)\right]\right\}. \quad (2.39)\end{aligned}$$

The non-dimensional dynamic equation for the perturbed surface profile $\hat{h}(\mathbf{q},t)$ can then be given by

$$\frac{\partial\hat{h}}{\partial t} = (-q^4+\epsilon^{*2}q^3)\hat{h} - q^2\mathcal{W}_{\mathbf{q}} - \epsilon^{*2}\sum_{\mathbf{q}'}\hat{h}(\mathbf{q}')\hat{h}(\mathbf{q}-\mathbf{q}')\Lambda(\mathbf{q},\mathbf{q}'). \quad (2.40)$$

Here the Fourier transform of the re-scaled wetting potential $W(h)/\mathcal{E}_0$,

$$\mathcal{W}_{\mathbf{q}} = -w * \left(\frac{h}{h^*_{ml}}\right)^{-\alpha_w} e^{-h/h^*_{ml}} \tag{2.41}$$

is used, and all the other terms have been calculated up to second order of surface perturbation. Also $\epsilon^* = \epsilon/\epsilon_0$ and

$$\begin{aligned}\Lambda(\mathbf{q},\mathbf{q}') &= q^2\left[(1-\nu)\frac{[\mathbf{q}'\cdot(\mathbf{q}-\mathbf{q}')]^2}{q'|\mathbf{q}-\mathbf{q}'|} - \mathbf{q}'\cdot(\mathbf{q}-\mathbf{q}') + \nu q'|\mathbf{q}-\mathbf{q}'|\right] \\ &+\frac{2q}{q'}\left\{q_x(q_x-q'_x)(q'^2_x+\nu q'^2_y) + q_y(q_y-q'_y)(q'^2_y+\nu q'^2_x)\right. \\ &\left.+(1-\nu)q'_xq'_y\left[q_x(q_y-q'_y)+q_y(q_x-q'_x)\right]\right\}. \end{aligned} \tag{2.42}$$

This recursive method can be applied to the third-order calculations and the results of elastic energy density $\hat{\mathcal{E}}^{(3)f}$ are shown in the appendix. The corresponding higher-order surface evolution equation can be obtained via adding term $-q^2\hat{\mathcal{E}}^{(3)f}$ to Eq. (2.40).

In the above evolution equation (2.40), the first term consists of the 1st order elastic energy $\hat{\mathcal{E}}^{(1)f}$ and the term obtained by the lowest order expansion of surface energy. This is consistent with the previous linear-order results [17, 59, 63]. The last term is from the nonlinear contribution of the elastic energy density, i.e., Eq. (2.37) for $\hat{\mathcal{E}}^{(2)f}$.

Using a similar process higher-order contributions can be obtained although they are much more complicated. In order to obtain the nth-order elastic results, we can first express the nth-order expansion of the boundary conditions in terms of ξth-order ($\xi = 1, 2, ..., n-1, n$) stress tensors [similar to the expression in Eq. (2.30)], and use it to calculate the nth-order solution of the displacement field given in Eq. (2.28); The corresponding film elastic properties can then be derived, particularly the nth-order elastic energy density $\hat{\mathcal{E}}^{(n)f}$ at the film surface which can be expressed as a function of ξth-order ($\xi = 1, 2, ..., n-1$) elastic quantities that are already known.

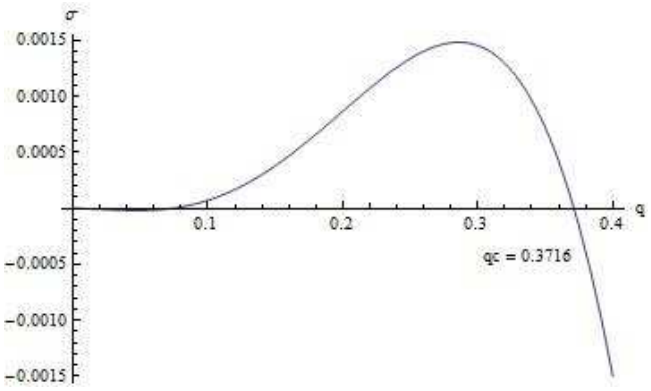

Figure 2.1. The growth rate of perturbation as a function of perturbation wavelength q for $\epsilon = 2\%$ with wetting potential parameters $w^* = 0.2, h^*_{ml} = 0.3$ and $\alpha_w = 2$

In this study,we only focus on Eq. (2.40) up to the 2nd-order elastic properties of nonlinear film evolution and strained island dynamics. We first determine the conditions of morphological instability of the system by performing a linear stability analysis of Eq. (2.40); such conditions are needed for the nonlinear calculations given in Sec. 3.1.

2.3 Linear analysis

In order to examine the detailed evolution of strained film morphology, we first consider the effect of the linear results on the surface morphology.

We Follow a standard procedure where we assume an exponential growth $\hat{h} = \hat{h}_0 \exp(\sigma_h t)$ at early time, and apply it to the linearized evolution equation of $\hat{h}$. The characteristic equation for the perturbation growth rate σ_h is then given by

$$\sigma_h = -q^4 + q^3 \epsilon^{*2} - q^2 a, \tag{2.43}$$

where $a = (w^*/h^*_{ml})(x + \alpha_w)x^{-\alpha_w - 1}e^{-x}$, $x = \bar{h}/h_{ml}$, $w^* = w/\mathcal{E}_0$, and $h^*_{ml} = h_{ml}/l$.

From figure 2.1 we can see that the growth rate rises to a maximum initially and then decreases, crossing the $\sigma = 0$ axis at the cutoff wave number,$q = q_c$. With the use

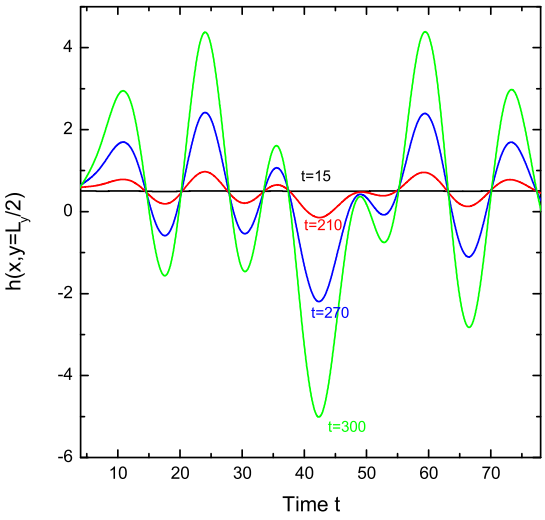

Figure 2.2. The 2D image of the variation of the surface height with x and fixed y at $y = L_y/2$.

of the wetting potential parameters $w^* = 0.2, h^*_{ml} = 0.3$ and $\alpha_w = 2$, for $\epsilon = 3\%, 2.5\%$ and $\epsilon = 2\%$ we find the cutoff wave numbers as 0.659, 0.4924 and 0.3716 respectively. It clearly shows that for the wave numbers smaller than q_c, the destabilization due to strain energy ($\propto q^3$) dominates and for wave numbers larger than q_c, the surface energy stabilization ($\propto q^4$) and the contribution from the wetting term ($\propto q^2$) dominates.

If we consider the effect of the linear results on the film surface, stability of film will not occur and we can see that film will grow with time. The variation of the height of the film surface with x and fixed y at $y = L_y/2$ for times $t = 15$, $t = 210$, $t = 270$ and $t = 300$ for $\epsilon = 3\%$ are shown in Fig. 2.2. It is clearly seen that the surface height increases with increasing time without saturation. In order to find the condition for the occurrence of the instability, we use the dispersion relation (2.43) and by setting $\frac{d\sigma_h}{dq} = 0$, and we can

find the condition for the instability as $\epsilon^{*4} \geq 4a$ or equivalently,

$$\frac{e^x x^{\alpha_w+1}}{x+\alpha_w} \geq \frac{4w^*}{\epsilon^{*4} h_{ml}^*}. \tag{2.44}$$

The corresponding characteristic wave number of film instability (for the fastest instability growth mode) can be written as

$$q_{\max} = \frac{3}{8}\left[\epsilon^{*2} + \sqrt{\epsilon^{*4} - \frac{32}{9}a}\right]. \tag{2.45}$$

The instability condition (2.44) is used to identify the parameters in our numerical simulations, for which the initial film instability and hence the appearance of nonplanar surface morphology or islands are needed.

Chapter 3

Numerical simulations and results

3.1 Numerical method

In our numerical calculations, we use pseudospectral method [68] to solve the nonlinear equation with periodic spatial domain in both x and y directions. In order to generate a numerical approximation, we apply the discrete Fourier transform on $h(x, y, t)$ (Eq. (2.17)). Since our film morphological profile $h(x, y, t)$ is real, we can use the fact that complex conjugate of the amplitude of negative wave numbers are related to their counterparts with positive wave numbers; $\hat{h}(\mathbf{q}, t) = \hat{h}^*(-\mathbf{q}, t)$.

Here we consider only the case of periodic boundary conditions where we would use the condition $h(x + L_x, y + L_y, t) = h(x, y, t)$. We can then relate $\hat{h}(\mathbf{q}, t)$ to $h(x, y, t)$ through the Fourier transform by

$$\hat{h}(\mathbf{q}, t) = \frac{1}{L_x L_y} \int_0^{L_x} dx \int_0^{L_y} dy h(x, y, t) e^{(-iq_x x - iq_y y)}. \tag{3.1}$$

Here L_x and L_y are the dimensions of x and y respectively. In our numerical approxima-

tion, we use the regular grid

$$\begin{aligned} x_i &= \frac{(i-1)L_x}{N_x}, \qquad i = 1, ..., N_x \\ y_j &= \frac{(j-1)L_y}{N_y}, \qquad j = 1, ..., N_y, \end{aligned} \tag{3.2}$$

and the wave numbers

$$\begin{aligned} q_x(i) &= \frac{2\pi i}{L_x} \qquad \text{for} - (N_x/2-1) \le i \le N_x/2 \\ q_y(j) &= \frac{2\pi j}{L_y} \qquad \text{for} - (N_y/2-1) \le j \le N_y/2. \end{aligned} \tag{3.3}$$

We then apply the Trapezoidal rule on to the equation Eq. (3.1) to get

$$\hat{h}(\mathbf{q}, t) = \frac{1}{N_x N_y} \sum_{i=1}^{N_x} \sum_{j=1}^{N_y} h(x_i, y_j, t) e^{-iq_x x_i} e^{-iq_y y_j}. \tag{3.4}$$

Let $\hat{N}$ be the nonlinear term and $\sigma_{\mathbf{q}} \hat{h}_{\mathbf{q}}$ be the linear term of the evolution equation Eq. (2.40);

$$\frac{\partial \hat{h}_q}{\partial t} = \sigma_{\mathbf{q}} \hat{h}_{\mathbf{q}} + \hat{N}_q \tag{3.5}$$

with

$$\sigma_h = -q^4 + q^3 \epsilon^{*2} - q^2 a, \tag{3.6}$$

and

$$\begin{aligned} \hat{N}_q \quad &= \epsilon^{*2} \sum_{\mathbf{q}'} \left\{ q^2 \left[(1-\nu) \frac{[\mathbf{q}' \cdot (\mathbf{q} - \mathbf{q}')]^2}{q' |\mathbf{q} - \mathbf{q}'|} - \mathbf{q}' \cdot (\mathbf{q} - \mathbf{q}') + \nu q' |\mathbf{q} - \mathbf{q}'| \right] \right. \\ &+ \frac{2q}{q'} \left[q_x (q_x - q'_x)(q'^2_x + \nu q'^2_y) + q_y (q_y - q'_y)(q'^2_y + \nu q'^2_x) \right. \\ &\left. \left. + (1-\nu) q'_x q'_y \left[q_x (q_y - q'_y) + q_y (q_x - q'_x) \right] \right] \right\} \hat{h}(\mathbf{q}') \hat{h}(\mathbf{q} - \mathbf{q}'). \end{aligned} \tag{3.7}$$

We evaluate the nonlinear term $\hat{N}_q$ by using the pseudospectral method in the Fourier space. We assume that this nonlinear term can be approximated by a linear function of t' in the interval $t \leq t' \leq t + \Delta t$ [68];

$$\hat{N} \approx \hat{N}_0 + \hat{N}_1(t - t') \tag{3.8}$$

where

$$\begin{aligned} \hat{N}_0 &= \hat{N}_q(t) \\ \hat{N}_1 &= \frac{\hat{N}_q(t + \Delta t) - \hat{N}_q(t)}{\Delta t}. \end{aligned} \tag{3.9}$$

We use this procedure to integrate the nonlinear term. We then have the final algorithm in the form [68]

$$\begin{aligned} \hat{h}_q(t + \Delta t) = e^{\sigma_{\mathbf{q}} \Delta t} \hat{h}_q(t) + \hat{N}_{\mathbf{q}}(t) \left[\frac{e^{\sigma_{\mathbf{q}} \Delta t} - 1}{\sigma_{\mathbf{q}}} \right] \\ + \frac{\hat{N}_q(t + \Delta t) - \hat{N}_q(t)}{\Delta t} \left[\frac{e^{\sigma_{\mathbf{q}} \Delta t} - (1 + \sigma_{\mathbf{q}} t)}{\sigma_{\mathbf{q}}^2} \right]. \end{aligned} \tag{3.10}$$

When $\sigma_{\mathbf{q}} \to 0$ we can rearrange the terms by taking the power serires of the exponential term as

$$\begin{aligned} \tfrac{e^{\sigma_{\mathbf{q}} \Delta t} - 1}{\sigma_{\mathbf{q}}} &= \Delta t \left[1 + \tfrac{1}{2} \sigma_{\mathbf{q}} \Delta t (1 + \tfrac{1}{3} \sigma_{\mathbf{q}} \Delta t + \tfrac{1}{12} \sigma_{\mathbf{q}}^2 \Delta t^2) \ldots \right] \\ \tfrac{e^{\sigma_{\mathbf{q}} \Delta t} - (1 + \sigma_{\mathbf{q}} \Delta t)}{\sigma_{\mathbf{q}}^2 \Delta t} &= \tfrac{1}{2} \Delta t (1 + \tfrac{1}{3} \sigma_{\mathbf{q}} \Delta t (1 + \tfrac{1}{4} \sigma_{\mathbf{q}} \Delta t)) + \ldots . \end{aligned} \tag{3.11}$$

3.2 Results

3.2.1 Effect of the wetting potential

The numerical simulations of the dynamic equation (2.40) are carried out for small film-substrate misfit strains because, the continuum elasticity theory can be well applied in weak strain limits [45]. In the analysis we use pseudospectral method with periodic boundary conditions along the directions x and y and an exponential propagation algorithm for time integration , as described above [68]. We use a large time step $\Delta t = 1$, and a numerical grid spacing $\Delta x = \Delta y = 1$.

In a film/substrate epitaxial system, the change of material properties across interlayer interfaces is the main cause for wetting effect [62]. When a film is grown on a substrate, there can be a wetting interaction between the film and the substrate. Previous work has been carried out to find the wetting effect on single-layer strained film growth [59, 62] and for multilayers [26] by considering either the change of material properties such as surface tension across the interface [18] or the nonlinear effect of the material elasticity [25,26].

We first perform numerical simulation of Eq. (2.40) with only the first order linear term and the glued-layer wetting potential given in Eq. (2.7) in order to validate our model system and the nonlinear dynamic equation. In the absence of the 2nd-order elastic contribution, the elastic energy relaxation would dominate and we can see the islands growing continuously even in the presence of the wetting potential. In order to understand this process we used the same wetting potential approximation for the comparison and with all the other parameters remain unchanged. As seen in Fig. 3.1 (a) and (b) where we see the variation of the surface height for misfit 2.5% with initial thickness 0.5 for times $t = 1200$ and $t = 1600$ respectively, the rapid growth of the surface islands would occur without any slowing down or saturation. This is also clearly seen in

the corresponding 2D surface profile as shown in Fig. 3.2 where we can identify several features of the surface dynamics. One characteristic is the large mass transport of the film surface which leads to thinner film layer and much higher islands. This diffusion process would occur even with the consideration of the wetting potential as a result of the increasing dominance of the destabilization effect of the 1st-order elastic energy. Another characteristic would be the island migration or the coarsening process which can be controlled only by the second order elastic contribution. When the islands grow higher and higher, this process will blow up eventually and the applicability of the perturbation method will not be acceptable.

To further illustrate this instability we plot the variation of the maximum surface height with time (Fig. 3.3). This is consistent with previous work [63], where we see a monotanically increasing maximum surface height with time.

We then examine the effect of the wetting potential by studying the 2D and 3D morphological profiles via solving the nonlinear evolution equation without the incorporation of the wetting effect. We use the misfit, $\epsilon = 3\%$ and the initial film thickness $h0 = 0$ to see deep grooves or cusps formed in the stressed solid systems. In this study, we use two types of initial conditions; one with the random disturbance of the film thickness h_0 in a 128×128 system (Fig 3.4(a) and (b)), and the other with doubly-periodic sinusoidal surface profile $h = h_0 + 0.01[cos(q_{x0}x) + cos(q_{y0}y)]$ with a system size of $\lambda_{x0} \times \lambda_{y0}$ (Fig 3.4 (c) and (d)). Here $\lambda_{x0} = 2\pi/q_{x0}$ and $\lambda_{y0} = 2\pi/q_{y0}$ where we choose $q_{x0} = q_{y0} = 3/4\sqrt{2}$ which corresponds to the wave number of most linearly unstable mode. In this study, we use $\Delta t = 0.01$. In both the cases we see cusps or grooves formation and the rapid growth during film evolution as shown by the 3D surface profile in Fig. 3.4 (a) and (c) and the 2D cross section profile in Fig. 3.4(b) and (d). The results we obtained are consistent with the results of Spencer and Meiron [69] and Xiang and E [56].

We also study the strength of the wetting interaction by changing the parameters of

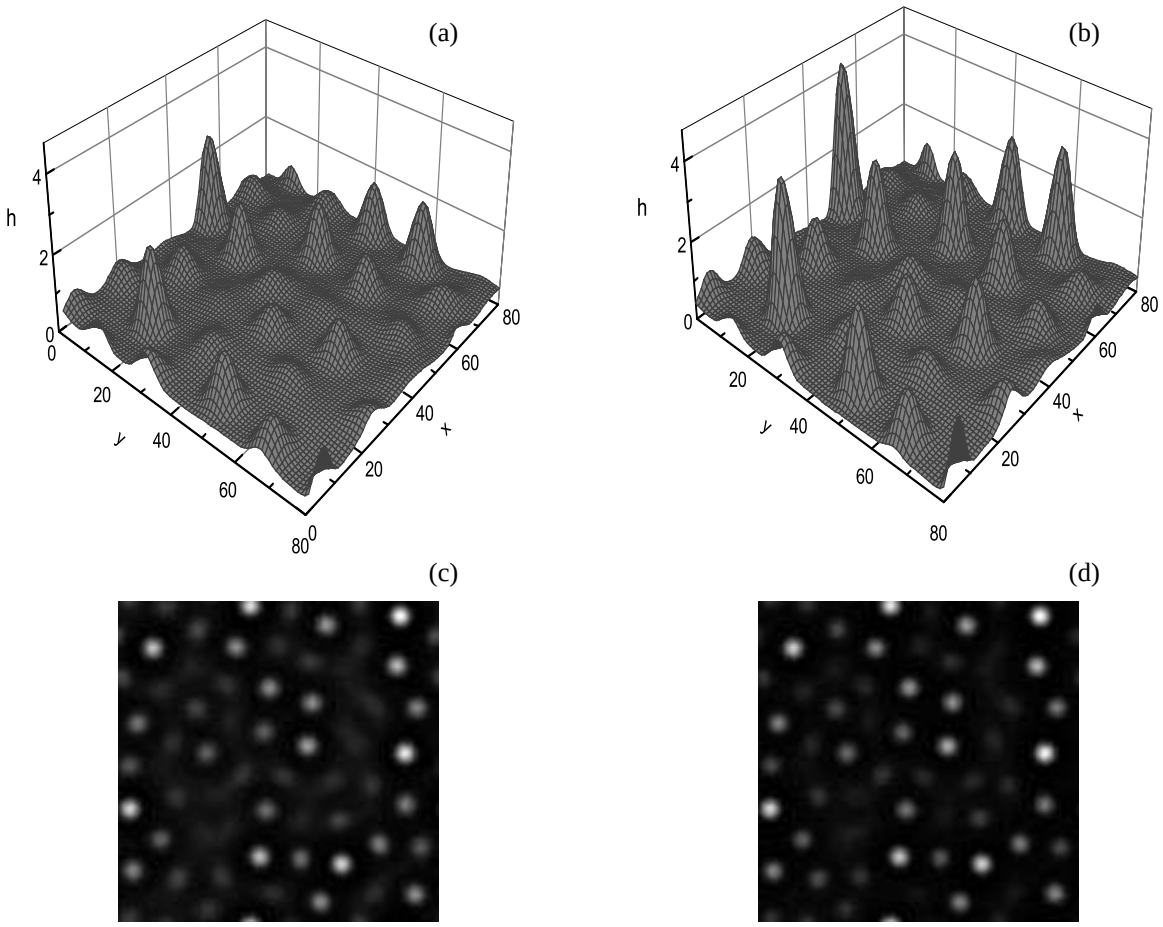

Figure 3.1. Morphological profiles and the the corresponding 2D gray scale top-view images of 2.5% strained films at times (a),(c) $t = 1200$ and (b),(d) $t = 1600$ with the considering of linear elastic energy contribution and wetting effect.

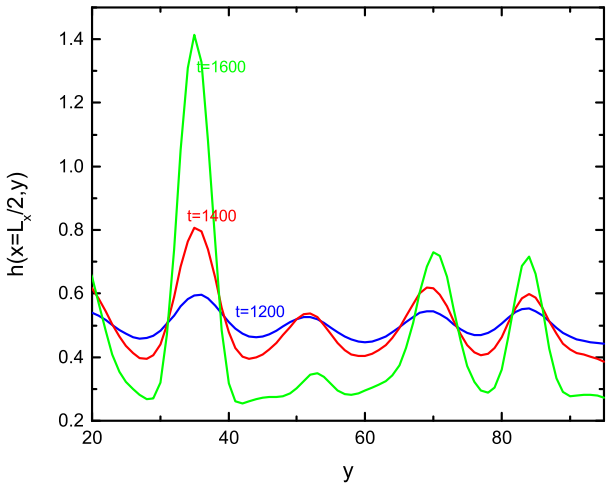

Figure 3.2. 2D morphological profiles of 2.5% strained films at times 1200, 1400 and 1600 obtained by considering the linear elastic energy contribution and wetting potential.

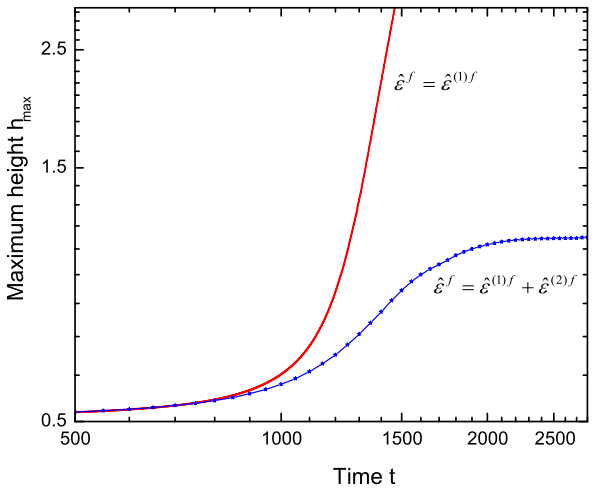

Figure 3.3. Maximum surface height as a function of time t for the two conditions where we consider results of the strained film evolution with first order elastic energy $\hat{\xi}^{(1)f}$ and the results from calculations up to 2nd-order elastic energy($\hat{\xi}^f = \hat{\xi}^{(1)f} + \hat{\xi}^{(2)f}$).

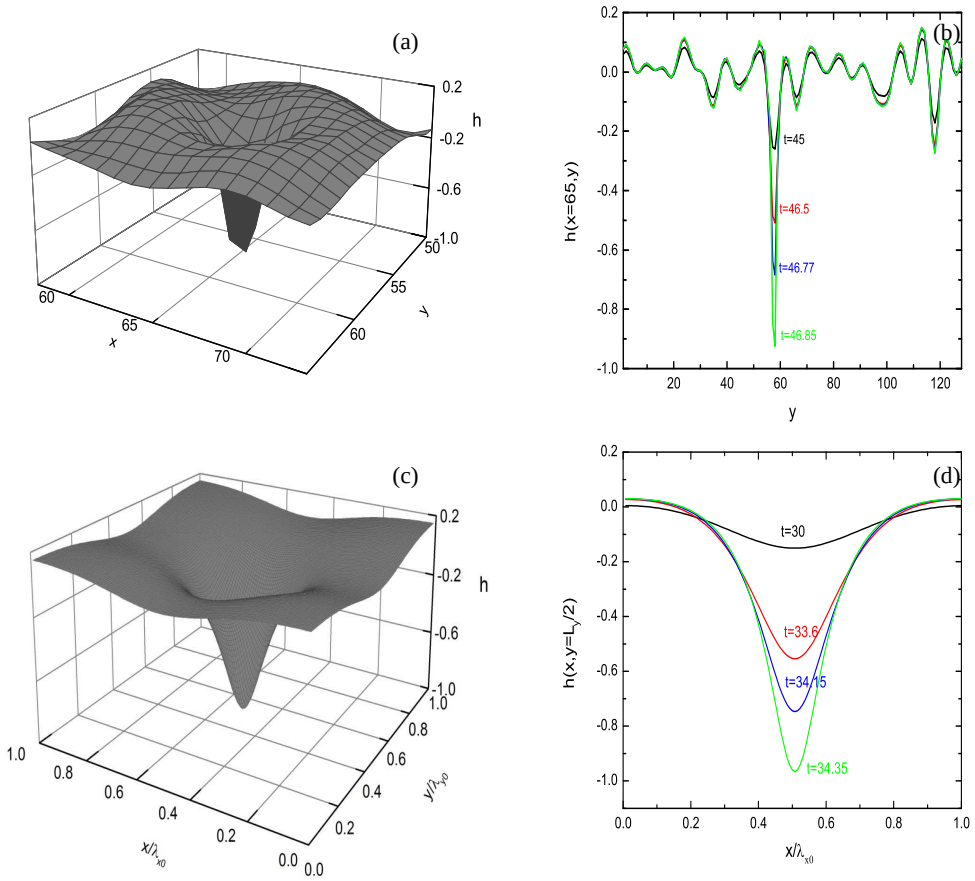

Figure 3.4. Surface morphologies of 3% strained films, as obtained from numerical simulations without the wetting effect. The simulations start either from small random initial perturbation of a planar film [(a) and (b)] or from a doubly-periodic surface profile with wave vector $q_{x0} = q_{y0} = 3/4\sqrt{2}$ and amplitude $A_0 = 0.01$ [(c) and (d)]. Both 3D morphologies, (a) at $t = 46.77$ for a portion of a 128×128 system and (c) at $t = 34.35$ for system size $\lambda_{x0} \times \lambda_{y0}$, and also time evolution of 2D cross-section profiles are shown.

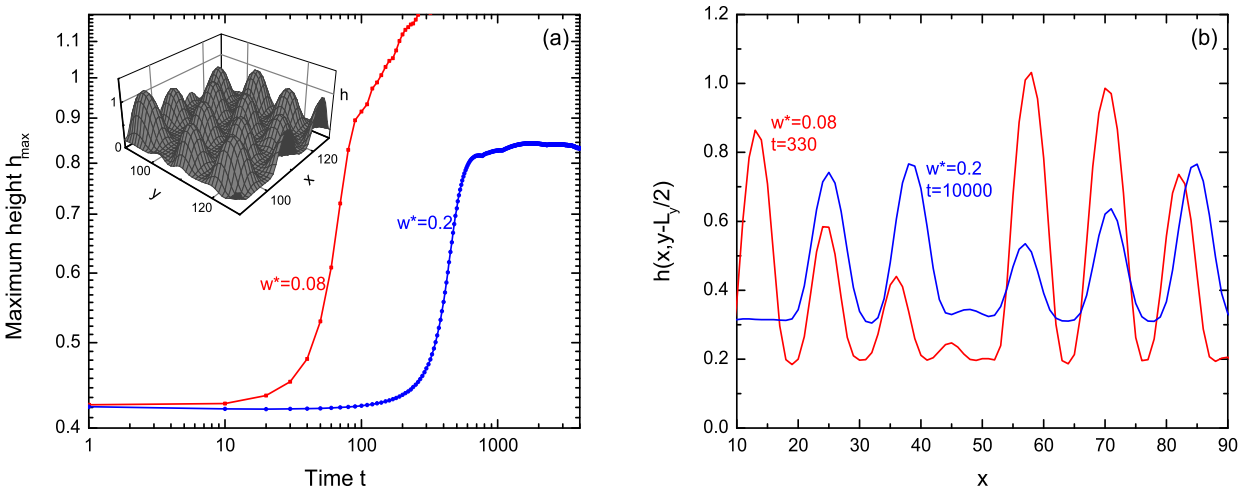

Figure 3.5. Time evolution of 3% strained films with different wetting strength $w^* = 0.08$ and 0.2. (a) Evolution of maximum surface height, with a 3D island morphology for $w^* = 0.08$ at $t = 330$ shown in the inset; (b) 2D cross-section profiles at $y = L_y/2$ for $w^* = 0.08$ at $t = 330$ and $w^* = 0.2$ at $t = 10000$.

the wetting potential. We changed the wetting interaction strength w^* by using $w^* = 0.08$ and $w^* = 0.2$ while the other parameters are $\epsilon = 3\%$, $h_0 = 0.41$, $\alpha_w = 2$ and the time step $\Delta t = 1$. Fig. 3.5 shows the comparison of the numerical results for weak and strong wetting interactions. When the strength of the wetting interaction is not strong enough, we see a rapid growth of the surface islands and the blow up of numerical solutions at later times, while stabilization and saturation of the surface islands are found for much stronger wetting potentials. This phenominan is clearly seen in Fig. 3.5 (a) showing the instability of the time evolution of the maximum surface height. This can be understood from the fact that the mass transport from the valleys to peaks increases when the wetting potential is not strong which leads to thinner wetting layer as seen in Fig. 3.5 (b). Much thicker film layers can be seen when the wetting interaction is strong (large w^*) which leads to a suppression on the valley-to-peak diffusion process.

3.2.2 Effects of nonlinearities on coarsening and saturation

The parameters that are assosiated with the nondimensional equation (2.40) is rescaled with the reference misfit $\epsilon_0 = 3\%$. If we use the material parameters of Si/Ge system, we find the estimated length scale as $l \simeq 5.5$ nm . The wetting potential parameters are chosen as $\nu = 1/3$, $h^*_{ml} = 0.3$, $w^* = 0.2$, and $\alpha_w = 2$. In this research we focus only on the nongrowing films with deposition rate $v = 0$. We simulate the annealing process of film evolution with the rescaled initial film thickness of $h_0 = 0.67$ for misfit strain $\epsilon = 2\%$, $h_0 = 0.5$ for $\epsilon = 2.5\%$, and $h_0 = 0.41$ for $\epsilon = 3\%$, all of which are within the corresponding instability parameter region for each misfit as determined by Eq. (2.44).

In order to understand the evolution of the surface morphology, we examine the dynamic equation (2.40) by conducting numerical simulations for three different misfit strains $\epsilon = 2\%, 2.5\%$ and 3%. In this simulation we use 3 different system sizes (128×128, 256×256, and 512×512) for each parameter set in order to examine any possible artifacts of finite size effect. In the systems 128×128 and 256×256, the quantitative results are averaged over 20 independent runs and in the system 512×512 they are averaged over 10 runs.

Fig. 3.6 illustrates the simulation results of formation and evolution of quantum dot arrays for 2.5% mismatch between the film and substrate. As shown in Fig. 3.6(a), strained surface islands or quantum dots are formed due to surface undulation which occurs at the beginning stage as a result of the film morphological instability determined in Eq. (2.44). Due to the effect of the nonlinear term on the elastic interaction, islands will form and grow gradually at different rates at different surface locations. The next stage is the coarsening of islands where some quantum dots grow at the expense of other shrinking ones by decreasing the island density on the film surface. This is clearly seen in Figs. 3.6(d)–(f) in the corresponding 2D top-view images when we compare the quantum

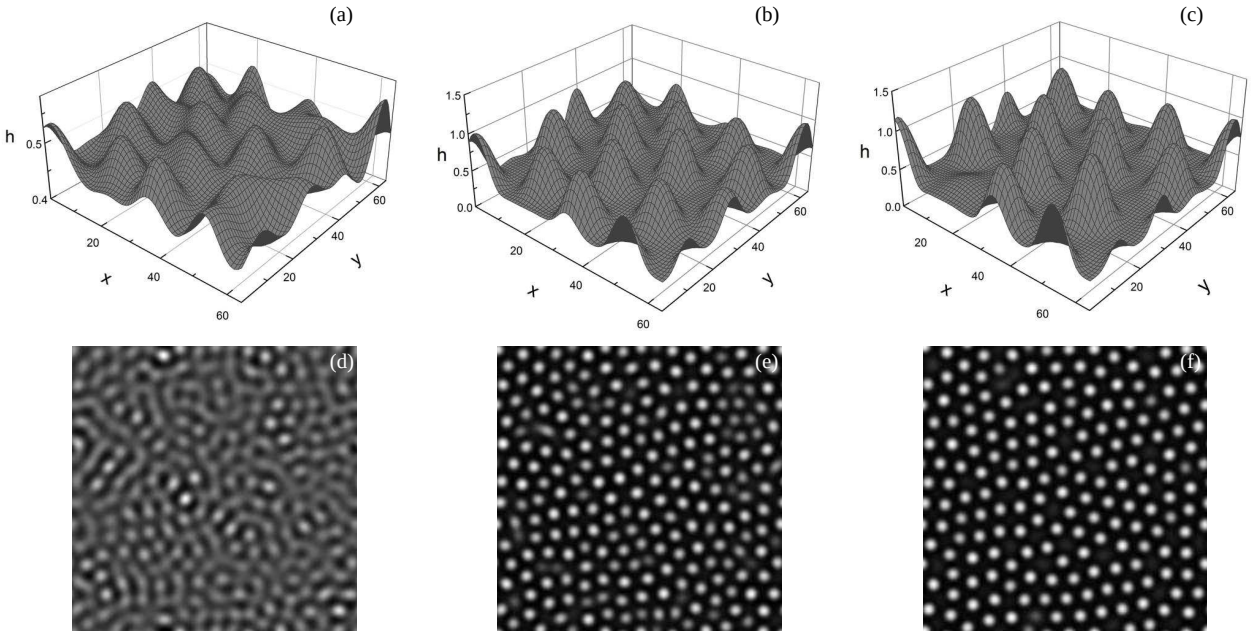

Figure 3.6. Morphological profiles for misfit 2.5% at times $t = 1000$ [(a) and (d)], 2000 [(b) and (e)], and 10000 [(c) and (f)]. Only a fraction of the system 256×256 is shown in the figures (a)-(c) with the corresponding 2D gray scale top-view images of the full size shown in (d)-(f).

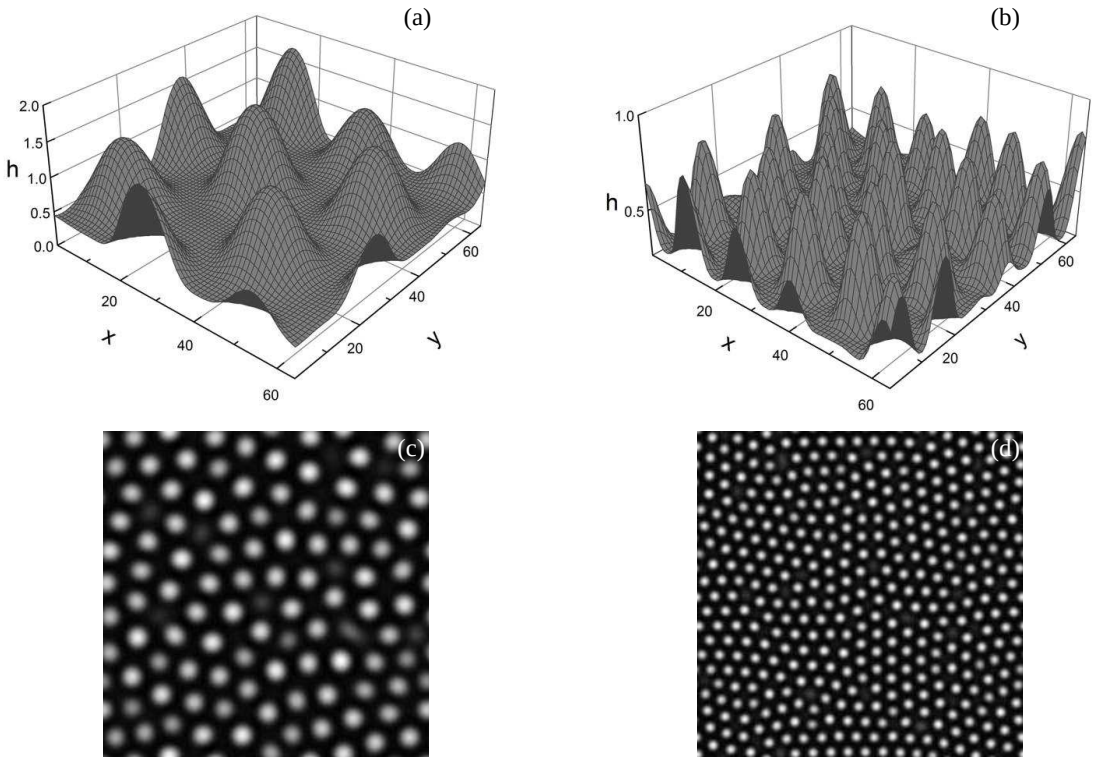

Figure 3.7. Morphological profiles for misfits (a) 2% and (b) 3% at late time stage of $t = 10000$. Only a portion of the 256×256 system is shown in the 3D images of (a) and (b). The corresponding 2D top-view images of the full system size are given in (c) and (d).

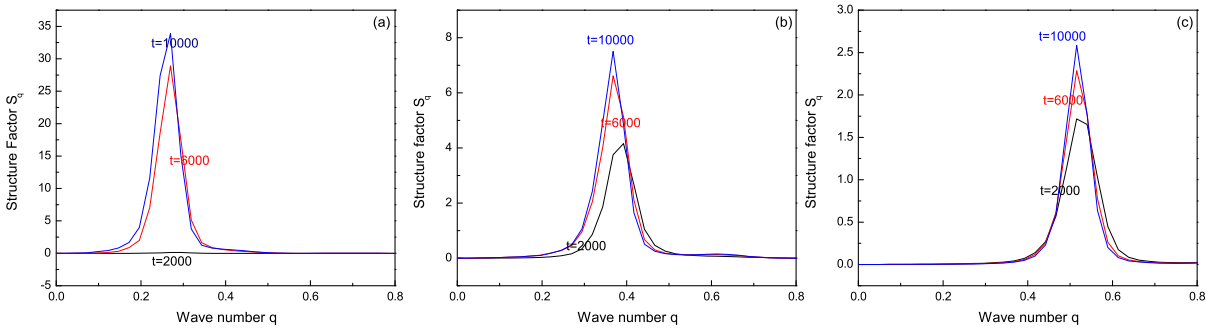

Figure 3.8. Structure factor of the surface height as a function of wave number q, for different misfits (a) $\epsilon = 2\%$, (b) $\epsilon = 2.5\%$, and (c) $\epsilon = 3\%$, system size 256×256, and times $t = 2000$, 6000, and 10000.

dot distribution for the times $t = 1000$, 2000, and 10000. As the time increases, this coarsening process becomes much slower and the system approaches to an asymptotic state with steady arrays of quantum dots. We have found that this film surface structure depends on the film-substrate misfit strain. As we increase the film-substrate misfit strain, the island density increases and the island spacing decreases. As shown in Fig. 3.7, our results of 2% and 3% confirm this as compared to the 2.5% film shown in Figs. 3.6(c) and 3.6(f). In our simulations no long-range spatial order can be found for quantum dot arrays, even at the late-time stage, agreeing with the observation of most experimental and theoretical studies.

To quantify these results, we study the structure factor $S(q,t) = \langle|\hat{h}(\mathbf{q},t)|^2\rangle_{\hat{q}}$. Here $\langle|\hat{h}(\mathbf{q},t)|^2\rangle_{\hat{q}}$ is the circular average over orientation of the wave vector. Figs. 3.8–3.11 show the variation of the structure factor, its moments, the maximum height of surface profile, and the surface roughness to analyze the film surface morphology. Fig. 3.8 shows the results of $S(q,t)$ for different misfit strains of 2%, 2.5%, and 3%. In this figure, we see that the wave number related to the peak location of the structure factor becomes larger as misfit increases. As a result, island spacing becomes smaller and also quantum dot

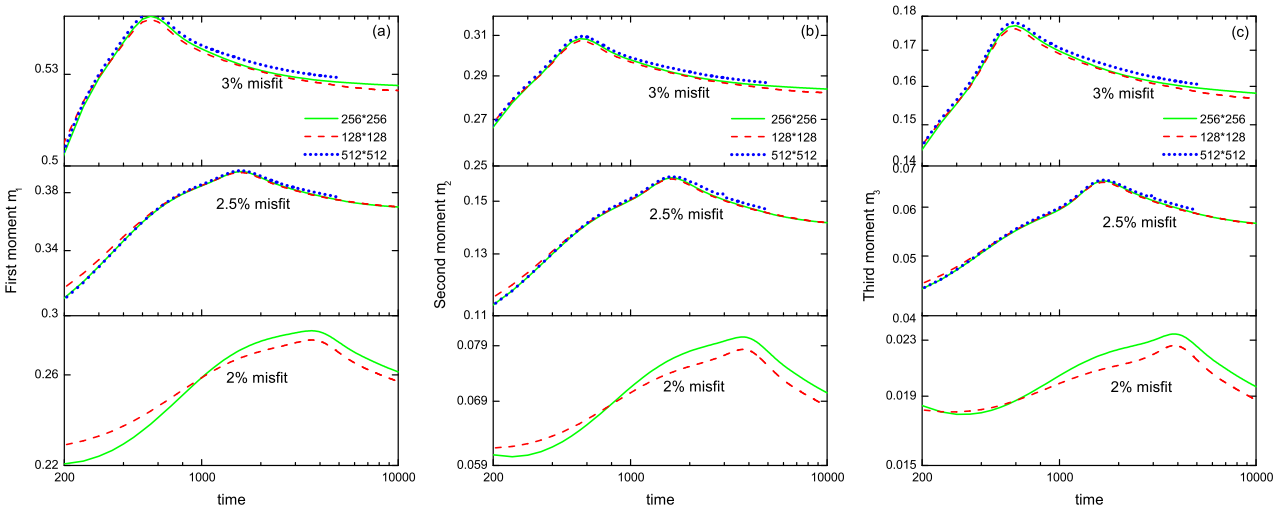

Figure 3.9. Time evolution of the three moments of structure factor: (a) m_1, (b) m_2, and (c) m_3, for misfit strains $\epsilon = 2\%$, 2.5%, and 3%. The solid lines represent the simulation results of grid size 256×256, whereas the dashed and dotted lines represent the results for grid sizes 128×128 and 512×512 respectively. Power law fittings (i.e., the thin lines) at the beginning of coarsening stage for the 256×256 system are also shown.

density increases. This is also seen in the Figs. 3.7(c), 3.6(f), and 3.7(d). Also, for the initial formation of islands, for smaller misfit strain larger time is needed (if we compare the $t = 2000$ curves in Figs. 3.8(a)–(c)), consistent with the result of σ_h in the linear stability analysis.

To characterize the details of the time evolution of quantum dots, we calculate the moments of the structure factor. The nth moment of $S(q,t)$ is defined as

$$m_n(t) = \frac{\int dq q^n S(q,t)}{\int dq S(q,t)}. \tag{3.12}$$

Using this moment, we can find the information of the characteristic size and spatial scale of surface structures. [71] For the three different misfits, we calculated the time evolution of the first three moments of $S(q,t)$. This is shown in Figs. 3.9(a) (for m_1), 3.9(b) (for m_2), and 3.9(c) (for m_3). In each simulation, we can see three characteristic

regimes of film evolution. During the early times, there is the process of surface instability developement and island formation as followed by the coarsening of these strained islands at the intermediate stage. These first two stages can be clearly distinguished in the results of moments shown in Fig. 3.9, as separated by the turning point (i.e., maximum of m_n) of the time evolution curve for each moment m_n. At late times, we see the asymptotic stage of island saturation. The reason for the increase of m_n at the initial stage is the continuous appearance of new islands at various times, and thus the decrease of average island spacing. Due to the overall smaller instability growth rate [see Eqs. (2.43)–(2.45)], the time range of this early stage of island formation is longer for smaller misfit strain. This can be also seen when we compare the three panels of misfits 3%, 2.5%, and 2% (from top to bottom) for results of each moment in Fig. 3.9.

After the formation, the islands start to coarsen with an increase of the average distance between islands, leading to the decrease of m_m. We can obtain a power-law behavior of coarsening, $m_n(t) \sim t^{-\beta_n}$, but such behavior is limited to a transient time range at the beginning of the coarsening stage. This time range is smaller for larger film-substrate misfit strain ϵ, as shown in Fig. 3.9. We have also found that the larger the misfit, the slower the coarsening rate is, corresponding to smaller coarsening exponents β_n which are identified as (for system size 256×256): For $\epsilon = 2\%$, $\beta_1 = 0.1010 \pm 0.0008$, $\beta_2 = 0.181 \pm 0.002$, and $\beta_3 = 0.235 \pm 0.003$; For $\epsilon = 2.5\%$, $\beta_1 = 0.0702 \pm 0.0007$, $\beta_2 = 0.120 \pm 0.002$, and $\beta_3 = 0.145 \pm 0.004$; For $\epsilon = 3\%$, $\beta_1 = 0.0449 \pm 0.0009$, $\beta_2 = 0.076 \pm 0.003$, and $\beta_3 = 0.090 \pm 0.006$. If the structure factor is assumed to obey a simple dynamic scaling behavior due to coarsening, one would usually expect that $m_n(t) \sim t^{-n\beta_1}$; i.e., $\beta_n = n\beta_1$. However, these results that we have obtained for coarsening exponents in the intermediate/transient time range for all different misfit strains do not support this assumption, and we cannot identify a simple format of scaling for the structure factor. This might be due to the nonlinear relaxation of strain energy in the film and the

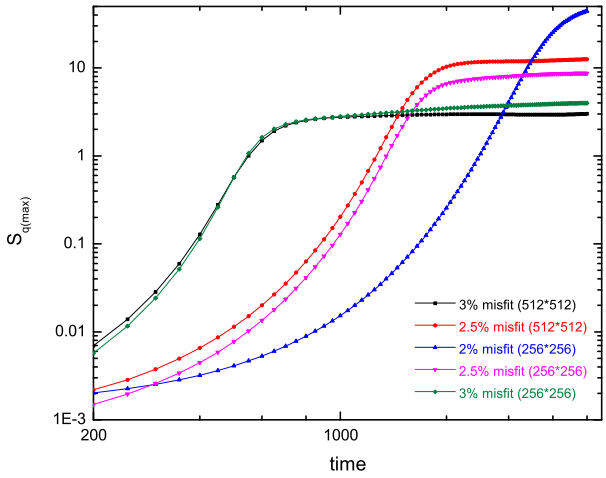

Figure 3.10. Time evolution of the maximum value of structure factor, for misfits $\epsilon = 2\%$, 2.5%, and 3%. Results for different system sizes 256×256 and 512×512 are shown for comparison.

nonlinear elastic interaction between surface islands [see e.g., Eq. (4.23)] which are more complicated than that revealed by simple scaling.

This island formation and coarsening can also be illustrated in our numerical results for the maximum value of the structure factor $S_{\max}$ (Fig. 3.10), the maximum surface height $h_{\max}$ (Fig. 3.11), and the surface roughness $r(t) = \langle (h - \bar{h})^2 \rangle^{1/2}$ (Fig. 3.12). In all these three quantities, we can see the first stage of instability growth and island formation which corresponds to the same initial time range as the m_n results in Fig. 3.9. Both $S_{\max}$ and the roughness $r(t)$ grow exponentially with time at this stage, consistent with the behavior of linear instability analysis. However, these quantities show rather slow growth and an approach to saturation at later times during the coarsening process, even for $h_{\max}$. Even though the phenomenon of surface roughness saturation has been obtained in a recent study of a nonlinear evolution equation, [62] no other studies have observed this phenomenon when using different evolution equations (which instead observed power-law

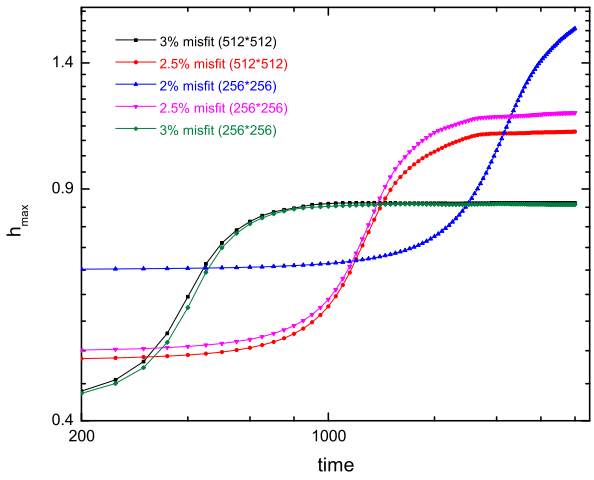

Figure 3.11. Time evolution of maximum surface height for misfits $\epsilon = 2\%$, 2.5%, and 3% and system sizes 256×256 and 512×512.

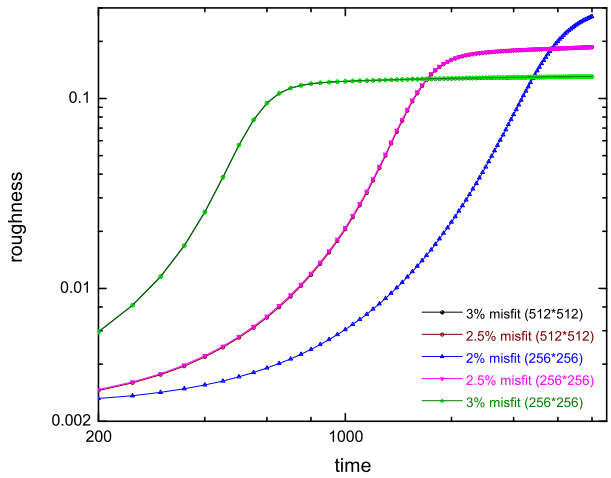

Figure 3.12. Time evolution of surface roughness for various misfits $\epsilon = 2\%$, 2.5% and 3%. Note that for each misfit, results of different system sizes 256×256 and 512×512 almost overlap with each other.

growth) [63,64]. The limited growth of maximum surface height given in Fig. 3.11 during island coarsening has not been reported in those previous studies, which usually showed faster growth of $h_{\max}$ such as a power-law behavior [63].

In our simulation results, we see a crossover from the island coarsening regime to an asymptotic state of steady quantum dot arrays, showing as saturated values of $S_{\max}$, $h_{\max}$, and $r(t)$ (see the 2.5% and 3% results in Figs. 3.10–3.12), and more clearly, the saturation of m_n given in Fig. 3.9. This crossover occurs earlier for larger misfit strain and corresponds to the slowing of the m_n decay after the transient of power-law-type coarsening. To check the finite size effect,we test on different system sizes ranging from 128×128 to 512×512 but obtained quantitatively similar results. This slowing and saturation of coarsening process is consistent with some experimental findings in Ge/Si systems [28, 32–34] and some modeling and simulation results based on either direct solution of system elasticity [53, 54, 61] or reduced film evolution equations; [62] however, no sign of coarsening termination in annealing films has been found in some other experimental [30] and theoretical [57,63,64] work. An important finding from our results, which is the effect of misfit strains on island coarsening and saturation, has not been studied in most previous works. We can suggest from the results that to observe the slowing or cessation of island coarsening for smaller misfits much longer times are needed. This could be useful for addressing the discrepancy of experimental observations. One example is that it is more difficult to observe the island saturation in SiGe/Si(001) experiments with weak misfit strain ($< 1\%$) [30], while the suppression or saturation of quantum dot growth can be found at relatively short annealing times for Ge/Si(001) system with large misfit ($\sim 4\%$) [28, 32, 33].

It would be useful to compare our calculations to previous theoretical work, particularly to that of Ref. [63] where the same wetting potential approximation Eq. (2.7) was adopted. They have found a power law coarsening behavior without any slowing or satu-

ration process observed. The main difference of their study and ours is the contribution of the system elasticity in the film evolution equation. In their model they have used only the linear elastic term while in ours we used the effect of nonlinear elasticity contribution up to 2nd order. Therefore we can argue that nonlinear contribution of the elastic energy plays a major role in determining the steady state of quantum dot arrays. There are also some other factors which paly an important role on island stabilization such as the anisotropy of surface energy which would lead to island shape/facet selection and transition, [28, 33], which will be addressed in our further studies. Note that our results are purely due to nonlinear elastic energy contribution while some previous theoretical studies (with various assumptions of the wetting effect), [53, 54, 61] have used the effect of surface energy anisotropy which also plays an important role on the existence of steady state island arrays.

The effect of the nonlinear interaction can be clearly seen in Fig. 3.2. We use the misfit 2.5% and the initial height of the surface profile as 0.5. If we consider only the linear interaction and the wetting potential, we see that the islands grow faster and diverge at small time period. More details of the important effect of higher-order elastic energy contribution will be given below.

3.2.3 Discussion

We study the time-varying profiles of the chemical potential $\mu = \gamma\kappa + W + \mathcal{E}^f$ and its corresponding elastic contribution $\mathcal{E}^f$ at the film surface to further illustrate the saturating process (Fig. 3.13 is for 2.5% misfit and at the cross section $x = L_x/2$). Smaller spatial variations of chemical potential μ along the film surface are obtained at later times [note the very small vertical scale in Fig. 3.13(a)], indicating an approach to an asymptotic saturated state. This is consistent with the results given in Figs. 3.9–3.12 for various

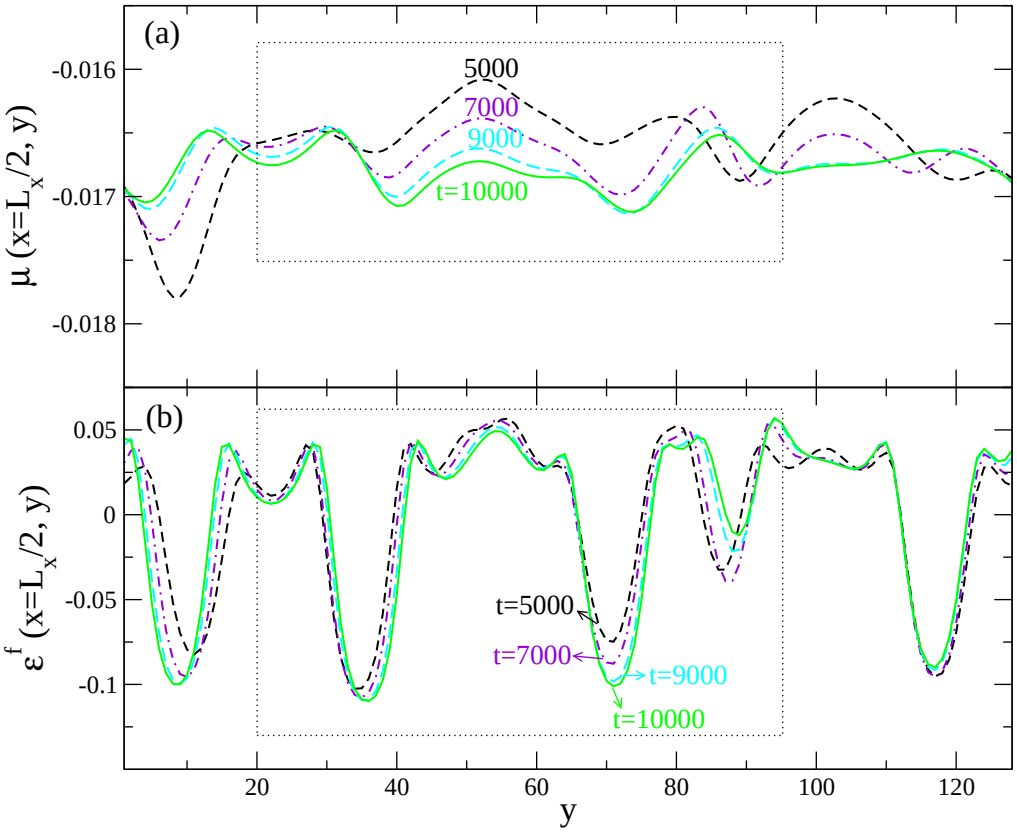

Figure 3.13. Cross-section profiles of (a) surface chemical potential μ and (b) elastic energy density $\mathcal{E}^f$, for misfit $\epsilon = 2.5\%$ and different times $t = 5000$, 7000, 9000, and 10000. The boxed region will be further studied in Fig. 3.14.

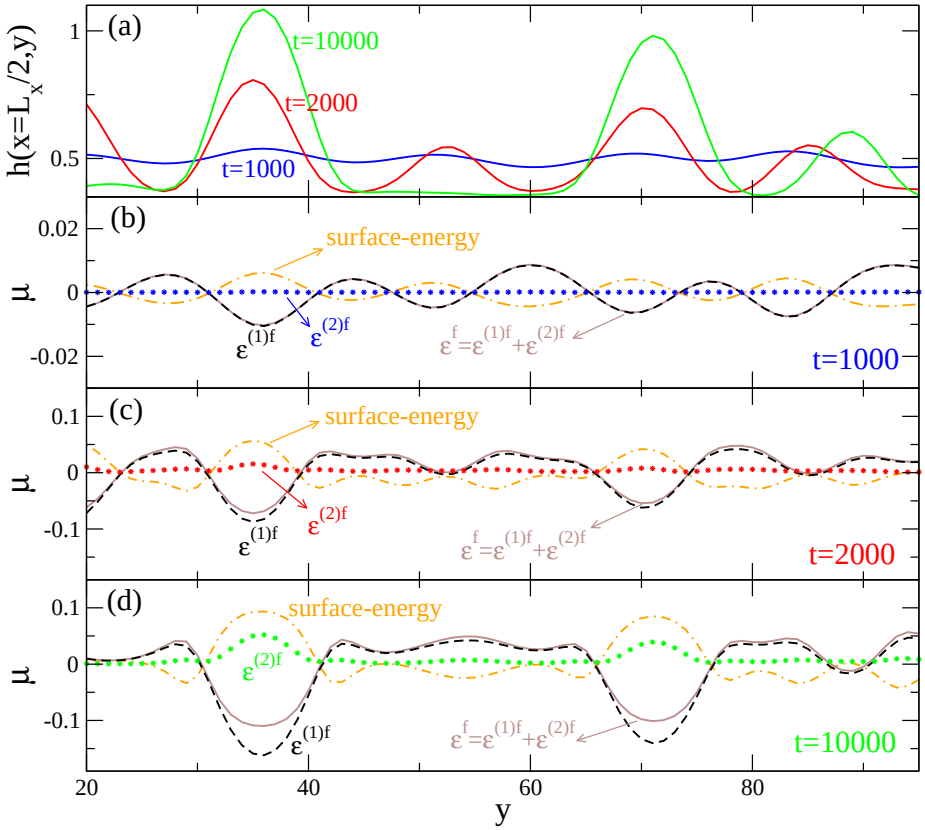

Figure 3.14. Cross-section profiles of (a) surface morphology and (b)-(d) various energy densities, for 2.5% misfit and times $t = 1000$ (at early stage of instability and island formation), 2000 (island coarsening stage), and 10000 (saturating stage). Different components of the film surface chemical potential are shown, including the surface-energy contribution (dot-dashed orange curves), 1st-order elastic energy density $\mathcal{E}^{(1)f}$ (dashed black), 2nd-order elastic density $\mathcal{E}^{(2)f}$ (green stars), and the total elastic contribution $\mathcal{E}^f = \mathcal{E}^{(1)f} + \mathcal{E}^{(2)f}$ (solid brown).

morphological properties, and also with the evolution profiles of elastic energy density $\mathcal{E}^f$ given in Fig. 3.13(b). Furthermore, in Fig. 3.14 we examine the detailed mechanisms of such saturation through identifying the time evolution of various components of chemical potential, including the surface-energy contribution $\gamma\kappa$ and the first and second order elastic energy densities $\mathcal{E}^{(1)f}$ and $\mathcal{E}^{(2)f}$. We focus on a small region of 4 islands [see Fig. 3.14(a)], representing 3 scenarios of quantum dot evolution: (1) large islands that are growing and saturating, (2) small islands that are shrinking [see the middle island in Fig. 3.14(a)], and (3) islands that are migrating (see the one at the right corner). As expected from previous analysis [17], for an undulated surface (i.e., in the region of surface islands), the strain energy is concentrated at surface valleys but released at peaks; the resulting surface elastic energy density gradient would drive the diffusion process from the valleys to peaks and thus the growth of surface islands. On the other hand, this morphological destabilization process is competed by the stabilization effect of surface energy, showing as energy penalty for high-curvature surface areas and hence a spatial distribution opposite to that of elastic density (see the dot-dashed curves). This classical view of quantum dot formation has been well reproduced in our results of all three evolution stages: the early morphological instability shown in Fig. 3.14(b) (at $t = 1000$), a coarsening regime in Fig. 3.14(c) (at $t = 2000$), and a saturating stage in Fig. 3.14(d) (at $t = 10000$).

For islands to be saturated and stabilized, one would expect mechanisms of film evolution involving additional energy penalty for large, increasing island size, so that the overall stabilization factors would compensate and suppress the destabilization effect (i.e., continuing growth and coarsening of surface islands) caused by stress relaxation. In previous studies such factors are usually provided by additional surface energy terms particularly the surface energy anisotropy, which has been shown to enhance the surface-energy stabilization effect, constrain the island height, and lead to island shape/facet selection and transition [33, 70]; this effect of surface anisotropy has been deemed essential for the exis-

tence of steady island arrays in some previous theoretical work (with various assumptions of the wetting effect) [53,54,61,67]. However, in this work we only consider isotropic surface energy. What we identify here is a new factor that is due to the contribution of higher-order perturbed elastic energy on the interaction and evolution of surface islands, as detailed in Fig. 3.14: Positive contribution from the 2nd-order elastic energy density $\mathcal{E}^{(2)f}$ is found for large surface islands, showing as an effective energy-penalty term and hence a reduction of strain relaxation effect. [Note that this result is still compatible with the well-known strain relaxation mechanism, since the total elastic density $\mathcal{E}^{f}$ still shows a destabilization effect due to the dominance of 1st-order density $\mathcal{E}^{(1)f}$; see Figs. 3.14 (c) and (d).] Such effect of $\mathcal{E}^{(2)f}$ becomes important only at late stage with large enough islands, and is negligible for small ones, as seen from the comparison between Figs. 3.14 (b)-(d).

To understand this seemingly counter-intuitive result which is beyond the conventional view based on linear instability analysis, we examine the detailed expression of $\mathcal{E}^{(2)f}$ which, from Eqs. (2.37)–(4.23), is rewritten as

$$\mathcal{E}^{(2)f}(\mathbf{r}) = \epsilon^{*2}\left[f(h) + \int d\mathbf{r}' \int d\mathbf{r}'' h(\mathbf{r}')G(\mathbf{r}-\mathbf{r}', \mathbf{r}'-\mathbf{r}'')h(\mathbf{r}'')\right], \tag{3.13}$$

where

$$f(h) = |\nabla h|^2 + \nu\left(\mathcal{E}^{(1)f}/\epsilon^{*2}\right)^2 + (1-\nu)\sum_{i=1}^{3} g_i^2(h), \tag{3.14}$$

with $g_i(h)$ $(i = 1, 2, 3)$ the Fourier transform of $q_x^2\hat{h}/q$, $q_y^2\hat{h}/q$, and $\sqrt{2}q_xq_y\hat{h}/q$ respectively,

and

$$G(\mathbf{r}-\mathbf{r}',\mathbf{r}'-\mathbf{r}'') = \sum_{\mathbf{q},\mathbf{q}'} e^{i\mathbf{q}\cdot(\mathbf{r}-\mathbf{r}')+i\mathbf{q}'\cdot(\mathbf{r}'-\mathbf{r}'')}$$
$$\times\frac{2}{qq'}\left\{q_x(q_x-q'_x)(q'^2_x+\nu q'^2_y)+q_y(q_y-q'_y)(q'^2_y+\nu q'^2_x)\right.$$
$$\left.+(1-\nu)q'_xq'_y\left[q_x(q_y-q'_y)+q_y(q_x-q'_x)\right]\right\}. \tag{3.15}$$

In Eq. (3.13), the first part $f(h)$ is always positive, analogous to the "self" elastic energy of a given surface profile that serves as a energy penalty to suppress its coarsening; the 2nd part represents the correlation between surface heights and thus the elastic interaction between surface islands. Within each island region (particularly near the peak), the magnitudes of both parts increase with the island size as verified in our numerical calculations.

If these 2nd-order elastic contributions are absent or not strong enough, the elastic energy relaxation would increasingly dominate over the surface-energy stabilization effect, driving the continuing island growth even in the presence of the wetting potential. This can be illustrated clearly from our numerical results given in Fig. 3.2, where the same film evolution equation (2.40) is simulated, but with only first-order elastic energy $\mathcal{E}^{(1)f}$ incorporated. All other parameters remain unchanged, including the same wetting potential approximation Eq. (2.7). The maximum surface height is found to increase monotonically with time [see Fig. 3.3], without any slowing or saturation process observed, a result that is consistent with previous work [63]. Time evolution of the corresponding 2D cross-section surface profiles is given in Fig. 3.3, from which two main features of surface dynamics can be identified: (1) Large mass transport from film layers to islands is observed, leading to much thinner film layers between surface islands as compared to the result shown in Fig. 3.14 (a) which incorporates the 2nd-order elastic energy

effects. Although the wetting potential still has the effect of preserving the wetting layer in-between surface islands and then limiting the diffusion process from the depleted wetting layer to the peaks, here such effect becomes relatively weaker as time evolves due to the increasing dominance of the destabilization effect of 1st-order elastic energy and the absence of "self" energy penalty term $f(h)$ for large islands. (2) Mass transport between islands continues to occur, which corresponds to island migration or coarsening process and is actually a secondary effect compared to (1). This process cannot be prevented by the wetting effect, and can be controlled only by the higher-order elastic energy terms describing island interaction and correlation [see Eq. (3.13)]. Thus at late times the island heights increase rapidly, resulting in the formation of surface islands with large aspect ratio between height and width as shown in Fig. 3.2. The perturbation method used here is no longer valid for such high islands, and the simulations will ultimately blow up. This is qualitatively different from the results given above with the incorporation of 2nd-order elastic energy, where islands with well constrained aspect ratio are obtained which also shows the applicability of the perturbation method developed here.

All these results indicate that the nonlinearities given by the higher-order strain energy of individual islands and the elastic interaction between islands can affect the pathway of film strain relaxation at late evolution times, slow down the decrease of total elastic energy via their increasing positive energy contribution for large islands, and thus effectively reduce the effect of stress relaxation as the surface instability driving force. Such reduction leads to relatively stronger role played by the surface energy and the wetting potential at later times [see the comparison between Figs. 3.14 (c) and (d), and between Figs. 3.14 (a) and 3.3], limiting the mass transport between film layers and islands and hence suppressing the island growth and coarsening.

Chapter 4

Effect of pre-patterned substrate on quantum dot growth

Formation of self assembled quantum dots on a pre-patterned substrate has attracted great interest due to the controllable positioning and perfect ordering of quantum dots arrays. In order to determine and predict island positioning and island sizes, factor that affect the arrangement of islands on patterned substrates such as lattice mismatch between the film and the substrate, surface energy and the substrate shape must be well understood. Here we consider the growth of strained islands on sinusoidal shape of substrate patterns with small and large amplitudes that can affect the size and shape of the grown islands. We need to address these factors and the dependency on the substrate pre-patterned amplitude to understand their effects on island growth, because, where these islands are formed and how to control the formation are not well understood in previous theoretical studies. In this study, we examine the dependency of the morphological instability and island properties on initial film thickness and the substrate pre-patterned amplitude.

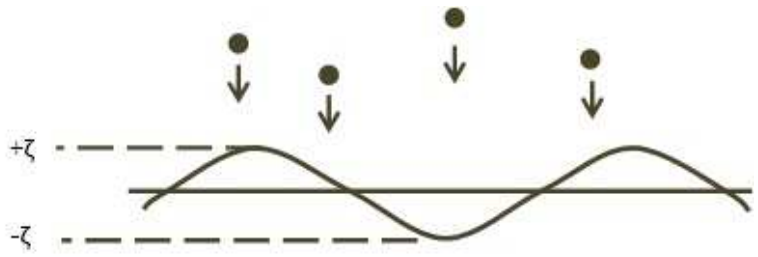

Figure 4.1. Nonplanar film-substrate interface

4.1 Continuum elasticity model with pre-patterned substrates

When we consider nonplanar or pre-patterned substrate (see Fig. 4.1), we assume that the substrate occupies the region $z < \zeta(x, y)$ and the film occupies the region $\zeta(x, yt) < z < h(x, y, t)$ with $\zeta(x, y)$ the profile of the film-substrate interface. We use the same mechanical equilibrium equation (Eq. (2.2)) as we used in the model with planar substrate. To the first order of perturbed quantities, the linearized boundary conditions at the film surface are given by

$$\begin{aligned} \hat{\sigma}_{xz}^{(1)f}(\mathbf{q}) &= iq_x\overline{\sigma}\hat{h}(\mathbf{q}), \\ \hat{\sigma}_{yz}^{(1)f}(\mathbf{q}) &= iq_y\overline{\sigma}\hat{h}(\mathbf{q}), \\ \hat{\sigma}_{zz}^{(1)f}(\mathbf{q}) &= 0. \end{aligned} \tag{4.1}$$

At the interface $z = \bar{\zeta} = 0$, the boundary conditions expanded to the 1st order are

$$\begin{aligned} -iq_x\bar{\sigma}\hat{\zeta}(\mathbf{q}) + \hat{\sigma}_{xz}^{(1)f}(\mathbf{q}) &= \hat{\sigma}_{xz}^{(1)s}(\mathbf{q}), \\ -iq_y\bar{\sigma}\hat{\zeta}(\mathbf{q}) + \hat{\sigma}_{yz}^{(1)f}(\mathbf{q}) &= \hat{\sigma}_{yz}^{(1)s}(\mathbf{q}), \\ \hat{\sigma}_{zz}^{(1)f}(\mathbf{q}) &= \hat{\sigma}_{zz}^{(1)s}(\mathbf{q}). \end{aligned} \tag{4.2}$$

and

$$\hat{u}_i^{(1)f} = \hat{u}_i^{(1)s} \qquad \text{for } i = x, y,$$

$$\bar{u}\hat{\zeta}^{(1)} + \hat{u}_z^{(1)f} = \hat{u}_z^{(1)s}. \tag{4.3}$$

$$\tag{4.4}$$

With the use of the linearized boundary conditions, we can obtain the first order coefficients of the solution given in Eqs. (2.28) and (2.29) as,

$$q\alpha_z^{(1)} = -q\hat{\zeta}\bar{u}e^{-2q\bar{h}}\left[q\bar{h} + 2(1-\nu) - \frac{1}{2} + \frac{1}{2}e^{2q\bar{h}}\right] + q\hat{h}\bar{u}e^{-q\bar{h}}(1 - 2\nu + q\bar{h}),$$

$$q\beta_z^{(1)} = -q\hat{\zeta}\bar{u}e^{-2q\bar{h}}\left[q\bar{h} + 2(1-\nu) - \frac{1}{2} - \frac{1}{2}e^{2q\bar{h}}\right] + q\hat{h}\bar{u}e^{-q\bar{h}}(1 - 2\nu + q\bar{h}),$$

$$iq_x\alpha_x^{(1)} + iq_y\alpha_y^{(1)} = -q\hat{\zeta}\bar{u}e^{-2q\bar{h}}\left[-q\bar{h} + 2(1-\nu) - \frac{1}{2} + \frac{1}{2}e^{2q\bar{h}}\right] + q\hat{h}\bar{u}e^{-q\bar{h}}(2(1-\nu) + q\bar{h}),$$

$$iq_x\beta_x^{(1)} + iq_y\beta_y^{(1)} = -q\hat{\zeta}\bar{u}e^{-2q\bar{h}}\left[-q\bar{h} + (1-2\nu) + \frac{1}{2} - \frac{1}{2}e^{2q\bar{h}}\right] + q\hat{h}\bar{u}e^{-q\bar{h}}(2(1-\nu) + q\bar{h}),$$

and

$$C^{(1)} = D^{(1)} = -q\hat{\zeta}\bar{u}e^{-2q\bar{h}} + q\hat{h}\bar{u}e^{-q\bar{h}}. \tag{4.5}$$

Based on the above solutions, we calculate the 1st order perturbed elastic energy density as

$$\hat{\mathcal{E}}^{(1)f} = -\frac{2E(1+\nu)}{1-\nu}\epsilon^2 q\left(\hat{h}(\mathbf{q}) - e^{-q\bar{h}}\hat{\zeta}(\mathbf{q})\right). \tag{4.6}$$

Substituting the expansions (2.17)-(2.18) into the boundary conditions (2.13)-(2.16) and retaining up to 2nd order perturbed quantities, we obtain the same boundary con-

ditions as at the top of the surface, $z = h(x, y, t)$,

$$(1-2\nu)(\partial_z^2 - q^2)\hat{u}_j^{(\xi)} + iq_j\left[iq_x\hat{u}_x^{(\xi)} + iq_y\hat{u}_y^{(\xi)} + \partial_z\hat{u}_z^{(\xi)}\right] = 0, \qquad \text{for } j = x, y, \tag{4.7}$$

$$(1-2\nu)(\partial_z^2 - q^2)\hat{u}_z^{(\xi)} + \partial_z\left[iq_x\hat{u}_x^{(\xi)} + iq_y\hat{u}_y^{(\xi)} + \partial_z\hat{u}_z^{(\xi)}\right] = 0, . \tag{4.8}$$

The corresponding second order boundary conditions at the film-substrate interface $z = 0$ are as follows;

$$\begin{aligned} &-\sum_{\mathbf{q}'} i(q_x - q_x')[\hat{\sigma}_{jx}^{(1)f}(\mathbf{q}') - \hat{\sigma}_{jx}^{(1)s}(\mathbf{q}')]\hat{\zeta}(\mathbf{q}-\mathbf{q}') \\ &-\sum_{\mathbf{q}'} i(q_y - q_y')[\hat{\sigma}_{jy}^{(1)f}(\mathbf{q}') - \hat{\sigma}_{jy}^{(1)s}(\mathbf{q}')]\hat{\zeta}(\mathbf{q}-\mathbf{q}') \\ &+\hat{\sigma}_{jz}^{(2)f}(\mathbf{q}) = \hat{\sigma}_{jz}^{(2)s}(\mathbf{q}), \end{aligned} \tag{4.9}$$

and

$$\hat{u}_i^{(2)f} = \hat{u}_i^{(2)s} \qquad \text{for } i = x, y \tag{4.10}$$

with $j = x, y, z$.

The solutions to the mechanical equation (2.2)is given by Eqs. (2.28) and (2.29) with the second order coefficients determined by the above boundary conditions, i.e.,

$$\begin{aligned} q\alpha_z^{(2)} \;&= -e^{-q\bar{h}}\left[\frac{a_1^{(2)}q_x + b_1^{(2)}q_y}{2\mu q}(1-2\nu+q\bar{h}) - \frac{c_1^{(2)}}{2\mu}(2-2\nu+q\bar{h})\right. \\ &\left. -\frac{f_1^{(2)}e^{-q\bar{h}}}{4\mu(1-\nu)}\left[q^2\bar{h}^2 + 4(1-\nu)^2 + \frac{3-4\nu}{2}(e^{2q\bar{h}} - 1 + 2q\bar{h})\right]\right], \end{aligned} \tag{4.11}$$

$$q\beta_z^{(2)} = -e^{-q\bar{h}}\left[\frac{a_1^{(2)}q_x + b_1^{(2)}q_y}{2\mu q}(1-2\nu+q\bar{h}) - \frac{c_1^{(2)}}{2\mu}(2-2\nu+q\bar{h}) - \frac{f_1^{(2)}e^{-q\bar{h}}}{4\mu(1-\nu)}\left[q^2\bar{h}^2 + (1-2\nu)^2 + \frac{3-4\nu}{2}(e^{2q\bar{h}} - 1 + 2q\bar{h})\right]\right], \tag{4.12}$$

$$iq_x\alpha_x^{(2)} + iq_y\alpha_y^{(2)} = iq_x\beta_x^{(2)} + iq_y\beta_y^{(2)} = e^{-q\bar{h}}\left[\frac{a_1^{(2)}q_x + b_1^{(2)}q_y}{2\mu q}(q\bar{h} - 2 + 2\nu) + \frac{c_1^{(2)}}{2\mu}(1-2\nu+q\bar{h}) + \frac{f_1^{(2)}e^{-q\bar{h}}}{4\mu(1-\nu)\left[q^2\bar{h}^2 - 2(1-\nu)(1-2\nu)\right]}\right], \tag{4.13}$$

$$C^{(2)} = D^{(2)} = B^{(2)} = e^{-q\bar{h}}\left[-\frac{a_1^{(2)}q_x + b_1^{(2)}q_y}{2\mu q} + \frac{c_1^{(2)}}{2\mu} - \frac{f_1^{(2)}e^{-q\bar{h}}}{4\mu(1-\nu)}\left[q\bar{h} + 2(1-\nu) + \frac{1}{2}(e^{2q\bar{h}} - 1)\right]\right], \tag{4.14}$$

where

$$a_1^{(2)}q_x + b_1^{(2)}q_y = \sum_{\mathbf{q}'}\hat{h}(\mathbf{q}-\mathbf{q}')\hat{h}(\mathbf{q}')\left\{\frac{2E\epsilon}{q'(1-\nu)}\left[q_x(q_x-q_x')(q_x'^2 + \nu q_y'^2) + q_y(q_y-q_y')(q_y'^2 + \nu q_x'^2)\right] + 2E\epsilon\frac{q_x'q_y'}{q'}\left[q_x(q_y-q_y') + q_y(q_x-q_x')\right]\right\}, \tag{4.15}$$

$$c_1^{(2)} = \sum_{\mathbf{q}'}\hat{h}(\mathbf{q}-\mathbf{q}')\hat{h}(\mathbf{q}')\frac{E\epsilon}{1-\nu}\left[q_x'(q_x-q_x') + q_y'(q_y-q_y')\right]. \tag{4.16}$$

and

$$f_1^{(2)} = \sum_{\mathbf{q}'}\hat{\zeta}(\mathbf{q}-\mathbf{q}')\hat{\zeta}(\mathbf{q}')\frac{E\epsilon}{1-\nu}\left[q_x'(q_x-q_x') + q_y'(q_y-q_y')\right]. \tag{4.17}$$

In Fourier space, we write the second order correction to the free energy as

$$\begin{aligned}\hat{\mathcal{E}}^{(2)f} &= 2E\frac{(1+\nu)}{(1-\nu)}\sum_{\mathbf{q}'}\Big\{\Lambda(\mathbf{q},\mathbf{q}')\hat{h}(\mathbf{q}')\hat{h}(\mathbf{q}-\mathbf{q}')+2\epsilon^{*2}e^{-q'\bar{h}}\hat{h}(\mathbf{q}-\mathbf{q}')\hat{\zeta}(\mathbf{q}')\times\\ &\left[\frac{(q_x-q'_x)}{qq'}\left[q_x(q'^2_x+\nu q'^2_y)+(1-\nu)q'_xq'_yq_y\right]\right.\\ &+\frac{(q_y-q'_y)}{qq'}\left[q_y(q'^2_y+\nu q'^2_x)+(1-\nu)q'_xq'_yq_x\right]+\nu q'|\mathbf{q}-\mathbf{q}'|\\ &\left.+\frac{(1-\nu)}{q'|\mathbf{q}-\mathbf{q}'|}\left[\mathbf{q}'.(\mathbf{q}-\mathbf{q}')\right]^2\right]\\ &-\epsilon^{*2}\hat{\zeta}(\mathbf{q}')\hat{\zeta}(\mathbf{q}-\mathbf{q}')q^2\left[\frac{e^{-q'\bar{h}}}{2(1-\nu)}(q\bar{h}+1-2\nu)([\mathbf{q}'.(\mathbf{q}-\mathbf{q}')]^2)\right.\\ &\left.e^{-(\mathbf{q}'+|\mathbf{q}-\mathbf{q}'|)}\left[\frac{(1-\nu)}{q'|\mathbf{q}-\mathbf{q}'|}\left[\mathbf{q}'.(\mathbf{q}-\mathbf{q}')\right]^2+\nu q'|\mathbf{q}-\mathbf{q}'|\right]\right]\Big\}. \qquad (4.18)\end{aligned}$$

The above expressions can be made dimensionless using the length scale $l = 2\gamma(1-\nu)/3E(1+\nu)\epsilon^2$ and the time scale $\tau = 3l^4/4\gamma\Gamma_h$. Using the length scale and time scale, we can write the first order correction to the free energy density as

$$\hat{\mathcal{E}}^{(1)f} = q\epsilon^{*2}e^{-q\bar{h}}\zeta(\mathbf{q}) - q\epsilon^{*2}\hat{h}(\mathbf{q}) \qquad (4.19)$$

and the second order correction to the free energy as

$$\begin{aligned}\hat{\mathcal{E}}^{(2)f} &= \sum_{\mathbf{q}'}\Big\{\Lambda(\mathbf{q},\mathbf{q}')\hat{h}(\mathbf{q}')\hat{h}(\mathbf{q}-\mathbf{q}') + 2\epsilon^{*2}e^{-q'\bar{h}}\hat{h}(\mathbf{q}-\mathbf{q}')\hat{\zeta}(\mathbf{q}')\times \\ &\left[\frac{(q_x-q'_x)}{qq'}\left[q_x(q'^2_x+\nu q'^2_y)+(1-\nu)q'_xq'_yq_y\right]\right. \\ &+\frac{(q_y-q'_y)}{qq'}\left[q_y(q'^2_y+\nu q'^2_x)+(1-\nu)q'_xq'_yq_x\right]+\nu q'|\mathbf{q}-\mathbf{q}'| \\ &\left.+\frac{(1-\nu)}{q'|\mathbf{q}-\mathbf{q}'|}\left[\mathbf{q}'.(\mathbf{q}-\mathbf{q}')\right]^2\right] \\ &-\epsilon^{*2}\hat{\zeta}(\mathbf{q}')\hat{\zeta}(\mathbf{q}-\mathbf{q}')q^2\left[\frac{e^{-q'\bar{h}}}{2(1-\nu)}(q\bar{h}+1-2\nu)([\mathbf{q}'.(\mathbf{q}-\mathbf{q}')]^2)\right. \\ &\left.e^{-(\mathbf{q}'+|\mathbf{q}-\mathbf{q}'|)}\left[\frac{(1-\nu)}{q'|\mathbf{q}-\mathbf{q}'|}\left[\mathbf{q}'.(\mathbf{q}-\mathbf{q}')\right]^2+\nu q'|\mathbf{q}-\mathbf{q}'|\right]\right]\Big\}. \end{aligned} \tag{4.20}$$

Thus, we obtaine the dynamics of the surface profile as

$$\begin{aligned}\frac{\partial\hat{h}}{\partial t} &= (-q^4+\epsilon^{*2}q^3)\hat{h}-\epsilon^{*2}q^3e^{-q\bar{h}}\hat{\zeta}(\mathbf{q})-q^2\mathcal{W}_{\mathbf{q}} \\ &+q^2\sum_{\mathbf{q}'}\Big\{\Lambda(\mathbf{q},\mathbf{q}')\hat{h}(\mathbf{q}')\hat{h}(\mathbf{q}-\mathbf{q}')+2\epsilon^{*2}e^{-q'\bar{h}}\hat{h}(\mathbf{q}-\mathbf{q}')\hat{\zeta}(\mathbf{q}')\times \\ &\left[\frac{(q_x-q'_x)}{qq'}\left[q_x(q'^2_x+'^2_y)+(1-\nu)q'_xq'_yq_y\right]\right. \\ &+\frac{(q_y-q'_y)}{qq'}\left[q_y(q'^2_y+\nu q'^2_x)+(1-\nu)q'_xq'_yq_x\right]+\nu q'|\mathbf{q}-\mathbf{q}'| \\ &\left.+\frac{(1-\nu)}{q'|\mathbf{q}-\mathbf{q}'|}\left[\mathbf{q}'.(\mathbf{q}-\mathbf{q}')\right]^2\right] \\ &-\epsilon^{*2}\hat{\zeta}(\mathbf{q}')\hat{\zeta}(\mathbf{q}-\mathbf{q}')q^2\left[\frac{e^{-q'\bar{h}}}{2(1-\nu)}(q\bar{h}+1-2\nu)([\mathbf{q}'.(\mathbf{q}-\mathbf{q}')]^2)\right. \\ &\left.e^{-(\mathbf{q}'+|\mathbf{q}-\mathbf{q}'|)}\left[\frac{(1-\nu)}{q'|\mathbf{q}-\mathbf{q}'|}\left[\mathbf{q}'.(\mathbf{q}-\mathbf{q}')\right]^2+\nu q'|\mathbf{q}-\mathbf{q}'|\right]\right]\Big\}. \end{aligned} \tag{4.21}$$

For simplicity, we consider a substrate stripe pattern with one characteristic wave number $\mathbf{q}^* = (q^*_x, q^*_y))$ with $\hat{\zeta}(\mathbf{q}^*) = \zeta_0$, i.e.

$$\hat{\zeta}(q_x^*, q_y^*) = \begin{cases} \zeta_0 & \text{if } \mathbf{q} = \pm\mathbf{q}^*; \\ 0 & \text{otherwise.} \end{cases}$$

The dynamics of the surface profile is then given by

$$\begin{aligned} \frac{\partial \hat{h}}{\partial t} &= (-\frac{3}{4}q^4 + q^3)\hat{h} - q^2\mathcal{W}_{\mathbf{q}} \\ &+q^2 \sum_{\mathbf{q}'} \Lambda(\mathbf{q}, \mathbf{q}')\hat{h}(\mathbf{q}')\hat{h}(\mathbf{q} - \mathbf{q}') + f_1(\mathbf{q}, \mathbf{q}^*)\hat{h}(\mathbf{q} - \mathbf{q}^*) + f_2(\mathbf{q}, \mathbf{q}^*)\hat{h}(\mathbf{q} + \mathbf{q}^*) + f_3(\mathbf{q}, \mathbf{q}^*) \end{aligned} \tag{4.22}$$

with

$$\begin{aligned} \Lambda(\mathbf{q}, \mathbf{q}') &= q^2 \left[(1-\nu)\frac{[\mathbf{q}' \cdot (\mathbf{q} - \mathbf{q}')]^2}{q'|\mathbf{q} - \mathbf{q}'|} - \mathbf{q}' \cdot (\mathbf{q} - \mathbf{q}') + \nu q'|\mathbf{q} - \mathbf{q}'| \right] \\ &+\frac{2q}{q'} \left\{ q_x(q_x - q_x')(q_x'^2 + \nu q_y'^2) + q_y(q_y - q_y')(q_y'^2 + \nu q_x'^2) \right. \\ &\left. +(1-\nu)q_x'q_y' \left[q_x(q_y - q_y') + q_y(q_x - q_x') \right] \right\}, \end{aligned} \tag{4.23}$$

$$\begin{aligned} f_1(\mathbf{q}, \mathbf{q}^*) &= 2\zeta_0 q e^{-q^*\bar{h}} \left[qg(\mathbf{q}, \mathbf{q}^*) + \frac{1}{q^*} f(\mathbf{q}, \mathbf{q}^*) \right], \\ f_2(\mathbf{q}, \mathbf{q}^*) &= 2\zeta_0 q e^{-q^*\bar{h}} \left[qg(\mathbf{q}, -\mathbf{q}^*) + \frac{1}{q^*} f(\mathbf{q}, -\mathbf{q}^*) \right] \\ f_3(\mathbf{q}, \mathbf{q}^*) &= -\zeta_0 q^{*3} e^{-q^*\bar{h}} (\delta_{\mathbf{q},\mathbf{q}^*} + \delta_{\mathbf{q},-\mathbf{q}^*}) \\ &-2\zeta_0^2 q^{*4} e^{-2q^*\bar{h}} \frac{3 - 4\nu + 2q^*\bar{h}}{1-\nu} (\delta_{\mathbf{q},2\mathbf{q}^*} + \delta_{\mathbf{q},-2\mathbf{q}^*}) \end{aligned} \tag{4.24}$$

where

$$f(\mathbf{q},\mathbf{q}^*) = q_x(q_x - q_x^*)(q_x^{*2} + \nu q_y^{*2}) + q_y(q_y - q_y^*)(q_y^{*2} + \nu q_x^{*2})$$
$$+(1-\nu)q_x^* q_y^*[q_x(q_y - q_y^*) + q_y(q_x - q_x^*)],$$
$$g(\mathbf{q},\mathbf{q}^*) = (1-\nu)\frac{[\mathbf{q}^*.(\mathbf{q}-\mathbf{q}^*)]^2}{q^*|\mathbf{q}-\mathbf{q}^*|} + \nu q^*|\mathbf{q}-\mathbf{q}^*|. \tag{4.25}$$

In this study we determine the conditions of morphological instability of the system by performing a linear stability analysis on the dynamic equation (4.22) .

4.2 Linear analysis

Linear stability analysis for pre-patterned substrate is more complex than for the planar substrate. We can write the dynamic of the surface profile to the first order of $\hat{h}$ as

$$\frac{\partial \hat{h}(\mathbf{q})}{\partial t} = f_0(q)\hat{h}(\mathbf{q}) + f_1(\mathbf{q},\mathbf{q}^*)\hat{h}(\mathbf{q}-\mathbf{q}') + f_2(\mathbf{q},\mathbf{q}^*)\hat{h}(\mathbf{q}+\mathbf{q}') + f_3(\mathbf{q},\mathbf{q}^*) \tag{4.26}$$

where $f_0(q) = q^3 - \frac{3}{4}q^4$ if we neglect the wetting effect as applied to the analysis given below. The general linear equation of $\hat{h}$ can be written as

$$\frac{\partial \hat{h}(\mathbf{q}+j\mathbf{q}^*)}{\partial t} = f_0(q)\hat{h}(|\mathbf{q}+j\mathbf{q}^*|)\hat{h}(\mathbf{q}+j\mathbf{q}^*)$$
$$+f_1(\mathbf{q}+j\mathbf{q}^*,\mathbf{q}^*)\hat{h}(\mathbf{q}+(j-1)\mathbf{q}^*) + f_2(\mathbf{q}+j\mathbf{q}^*,\mathbf{q}^*)\hat{h}(\mathbf{q}+(j+1)\mathbf{q}')$$
$$+f_3(\mathbf{q}+j\mathbf{q}^*,\mathbf{q}^*), \tag{4.27}$$

with $j = -N, -N+1, \ldots, -1, 0, 1, \ldots, N-1, N$. For large values of q (i.e. $q >> 1$), we have $\hat{h}(\mathbf{q}) \to 0$. Therefore, at the boundary we can take $\hat{h}(\mathbf{q}+(N+1)\mathbf{q}') = \hat{h}(\mathbf{q}-(N+1)\mathbf{q}') = 0$ for $N >> 1$. In order to solve this linear equations we convert the differential

equations to a matrix form:

$$\frac{\partial}{\partial t}\begin{bmatrix}\hat{h}(-N)\\ .\\ .\\ .\\ \hat{h}(-1)\\ \hat{h}(0)\\ \hat{h}(1)\\ .\\ .\\ .\\ \hat{h}(N)\end{bmatrix} = \begin{bmatrix} f_0(-N) & f_2(-N) & 0 & ... & 0\\ . & & & & \\ . & & & & \\ . & & & & \\ 0 & 0 & 0 & ... & 0\\ 0 & 0 & 0 & ... & 0\\ 0 & 0 & 0 & ... & 0\\ . & & & & \\ . & & & & \\ . & & & & \\ 0 & 0 & 0 & ... & f_0(N)\end{bmatrix}\begin{bmatrix}\hat{h}(-N)\\ .\\ .\\ .\\ \hat{h}(-1)\\ \hat{h}(0)\\ \hat{h}(1)\\ .\\ .\\ .\\ \hat{h}(N)\end{bmatrix} + \begin{bmatrix}f_3(-N)\\ .\\ .\\ .\\ f_3(-1)\\ f_3(0)\\ f_3(1)\\ .\\ .\\ .\\ f_3(N)\end{bmatrix}$$

which is equivalent to:

$$\frac{\partial \overrightarrow{h}}{\partial t} = A\overrightarrow{h} + f_3 \tag{4.28}$$

We then can find the corresponding eigenvalues (σ_i) and the eigenvectors ($\overrightarrow{b}_i$) for the homogeneous equation

$$\frac{\partial \overrightarrow{h}_c}{\partial t} = A\overrightarrow{h}_c \tag{4.29}$$

and obtain the complementary solution for the $\overrightarrow{h}_c$,

$$\overrightarrow{h}_c(j) = \sum_i \overrightarrow{b}_i e^{\sigma_i t}. \tag{4.30}$$

This can now be written as

$$\hat{h}_c(j) = \sum_i b_{ij} e^{\sigma_i t} \tag{4.31}$$

with b_{ij} being the jth component of the eigenvector $\overrightarrow{b}_i$ which corresponds to the eigenvalue σ_i. For this analysis we consider the case where $j = 0$,

$$\hat{h}_c(\mathbf{q}) = \hat{h}(j = 0) = \sum_i b_{i0} e^{\sigma_i t}. \tag{4.32}$$

Therefore, finding the maximum component of the eigenvector $b_{i0(max)}$ with maximum perturbation growth rate σ_i for different wave vectors $q = (q_x, q_y)$results in finding the maximum wave number in the linear stability analysis. We use substrate stripe patterns with characteristic wave number $q_x^* = 0.5$ with fixed q_y^* at $q_y^* = 0$. For different amplitudes (ζ_0) of the substrate stripes at $\zeta_0 = 1, 1.2, 1.4$ and 1.6 we analyzed the effect of the initial film thickness h_0 on the instability growth rate to obtain the corresponding maximum wave number for the linear stability analysis. The relation between the periodicity of the pre-patterned substrate and of the grown islands is shown schematically in Fig. 4.2 We compare these results with the case of planar substrate pattern to understand the behavior of the pre-patterned substrate pattern. For the comparison, we use the condition for the occurrence of instability without considering the effect of the wetting potential. The corresponding dispersion relation for the planar substrate is,

$$\sigma_h = -\frac{3}{4}q^4 + q^3. \tag{4.33}$$

By setting $\frac{d\sigma_h}{dq} = 0$, we obtain that the condition for instability occurs when $q_{max} = 1$ at $\sigma_0 = 1/4$. Fig. (4.3) shows the variation of the eigenvector b_{i0} corresponding to the maximum instability growth rate for different initial thicknesses for a fixed substrate pattern amplitude ζ_0. The peak of each curve corresponds to the maximum value of the wave number.

When we increase the thickness of the film, the surface islands are less influenced

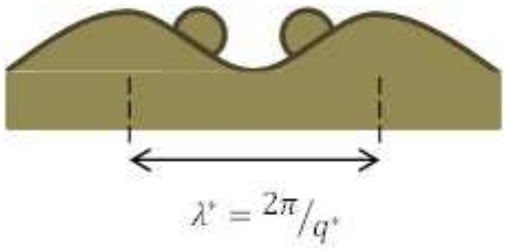

Figure 4.2. Schematic diagram of islands grown on pre-patterned substrate.

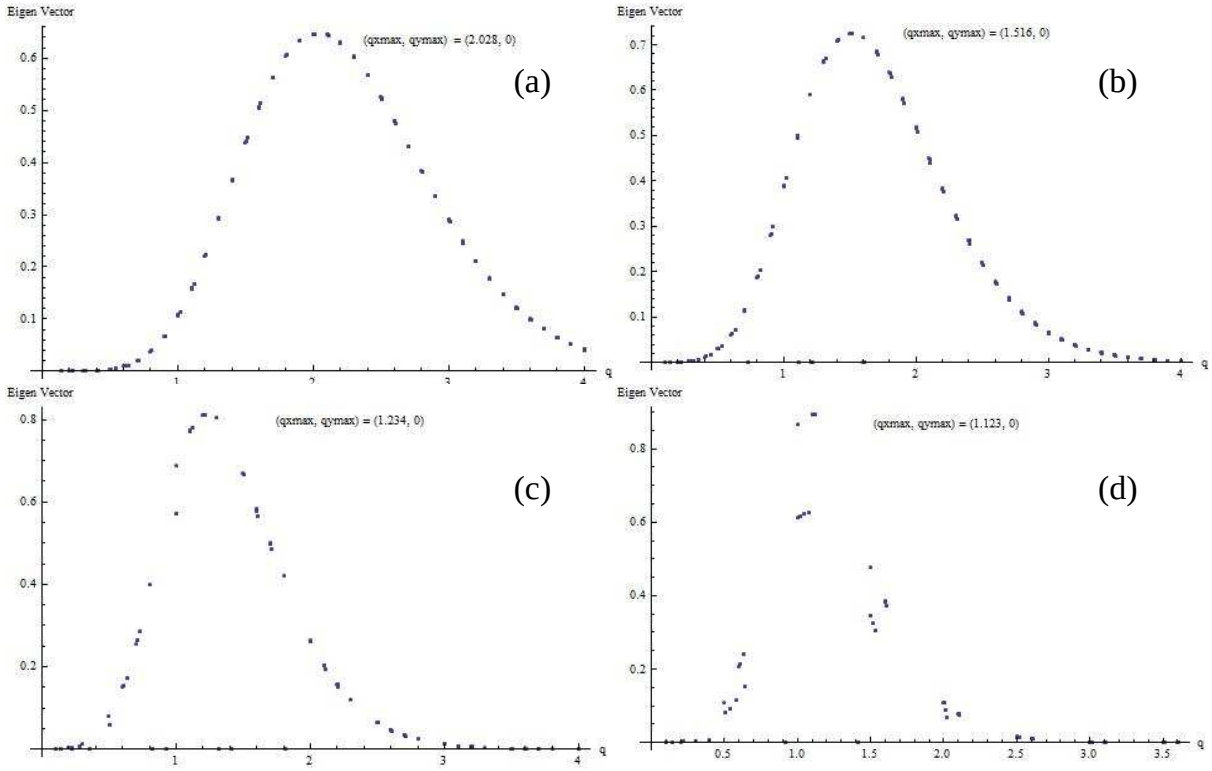

Figure 4.3. Variation of the eigenvector b_{i0} with respect to the wave number for various initial film thickness (a)$h_0 = 3$, (b)$h_0 = 4$, (c)$h_0 = 5$ and (d)$h_0 = 6$ for a fixed substrate pattern amplitude $\zeta_0 = 1.6$ and a fixed substrate pattern wave number $q_x* = 0.5, q_y* = 0$.

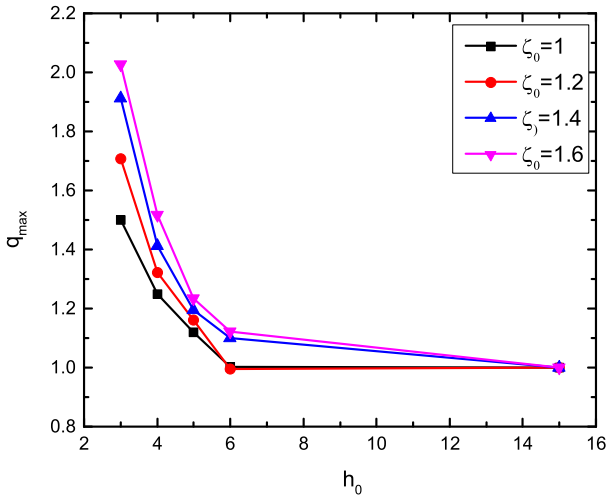

Figure 4.4. Variation of the maximum wave number with respect to the initial thickness of the film for different substrate wave patterns at $\zeta_0 = 1, 1.2, 1.4$ and 1.6. Here we used the wave number of the substrate pre-pattern $q_X^* = 0.5$ and $q_y^* = 0$.

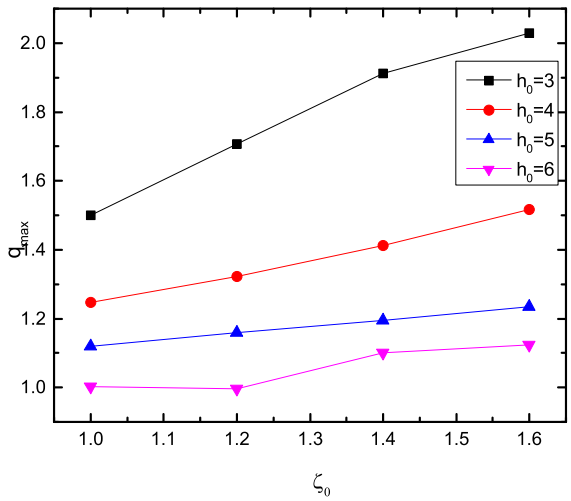

Figure 4.5. Variation of the maximum wave number with respect to the substrate pre=pattern amplitude for different initial film thicknesses at $h_0 = 1, 1.2, 1.4$ and 1.6

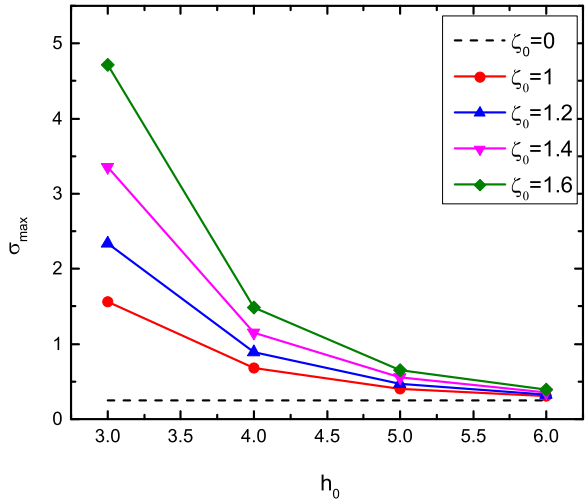

Figure 4.6. Variation of the maximum perturbation growth rate with respect to initial film thickness for different substrate wave patterns at $\zeta_0 = 1, 1.2, 1.4$ and 1.6. The dashed line represents the maximum growth rate ($\sigma_{max} = 1/4$) for a planar substrate.

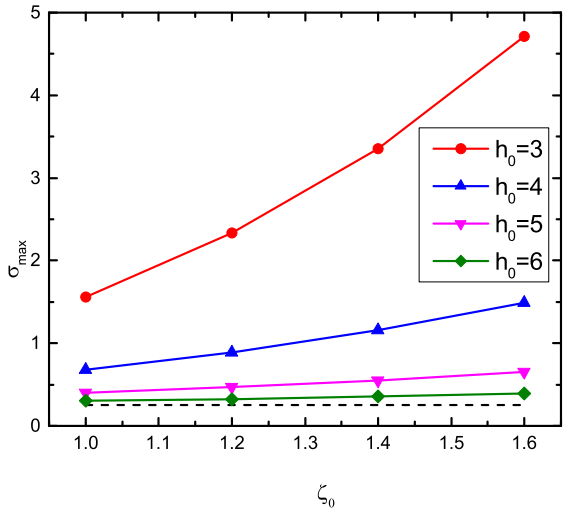

Figure 4.7. Variation of the maximum perturbation growth rate with respect to substrate pre-pattern amplitude for different initial film thicknesses at $h_0 = 1, 1.2, 1.4$ and 1.6. The dashed line represents the maximum growth rate ($\sigma_{max} = 1/4$) for a planar substrate.

by the substrate pattern. As a result, the maximum wave number corresponding to the morphological instability of the film surface would approach to the results of a planar substrate when h_0 increases. Also, if we increase the substrate pre-pattern amplitude, the effect from the substrate would lead to larger film instability wave number. This can be clearly seen in figures 4.4 and 4.5. Same scenario can be explained when we study the effect of the film thickness and the substrate pattern amplitude on the maximum perturbation growth rate (σ_{max}), as seen in figures 4.6 and 4.7. As we increase the film thickness, the effect of the substrate is negligible so $q_{max} \rightarrow 1$ which is the maximum film instability wave number in the planar substrate. The difference between the maximum wave number and the substrate pre-pattern q^* (here we used $q^* = 0.5$) increases with decreasing h_0. As a result we see larger island wavenumber for smaller film thicknesses.

Chapter 5

Conclusions

We have investigated the nonlinear dynamic processes governing the formation, coarsening, and stabilization of strained quantum dot islands on the surface of heteroepitaxial films, through the development of a nonlinear evolution equation for film morphology. Our study is based on a continuum elasticity model that incorporates the film-substrate wetting effect and importantly, on the construction of a perturbation method in Fourier space for determining the system elastic properties. In addition to a linear stability analysis which yields the conditions of film morphological instability, we have performed large scale numerical calculations of the dynamic equation derived to study the detailed behavior of film evolution. We focus on effects of small misfit strains which correspond to relatively large length scale of surface nanostructures, and analyze the evolution of strained surface islands/dots using a variety of characteristics of film morphology, including the structure factor of surface height, its first three moments, the maximum height of surface profile, and the surface roughness.

Consistent with previous experimental and theoretical work, our results have shown three characteristic stages of island evolution for post-deposited annealing films in the case of planar substrate, including (1) the early stage of morphological instability and island

formation, as characterized by the exponential growth of maximum structure factor $S_{\max}$ and the surface roughness as well as the increase of maximum surface height and moments m_n; (2) a nonlinear island coarsening stage, with a transient power-law behavior of m_n decay that appears at the beginning of this stage; and (3) a crossover to an asymptotic state of saturated island arrays (although without long-range spatial order), after the slowing and suppression process of coarsening. Also, the dependence of these detailed properties on the film-substrate misfit strain has been obtained, such as the values of coarsening exponents and the time ranges for the crossover between different evolution stages. These have been shown important for the understanding of different, or seemingly inconsistent, experimental results particularly for the late time stage of island coarsening or stabilization. On the other hand, such dependence does not qualitatively affect our results of the three evolution regimes; same conclusion can be drawn for the effect of different finite system sizes used in our simulations. To understand the mechanisms underlying the nonlinear evolution of strained films, we have examined the effects of film-substrate wetting potential, in particular its role on the suppression of the valley-to-peak mass diffusion process that would lead to wetting layer depletion, and its constraining effect on island growth. Furthermore, through a detailed study of time evolution of elastic energy density distribution at the film surface, we find that higher-order terms of film elastic energy, which incorporate the interaction between strained surface islands and the higher-order "self" elastic energy of individual islands, can effectively alter the relaxation pathway of film strain energy at late stage. They play an important role on the saturation and stabilization of quantum dot arrays, in particular the crossover to the saturated state with balanced multi-island interactions and limited island-layer and between-island mass transport. Thus our results indicate that both effects of film-substrate wetting interaction and high-order elastic energy are pivotal for the achieving of steady quantum dot arrays and also for the understanding of self-assembly process of strained film heteroepitaxy.

In the case of pre-patterned substrates, the morphological instability depends on the initial film thickness and the substrate pattern amplitude. Larger film instability wave number could be found for increasing film thickness, due to less influence of the substrate pattern on the morphological profile of an epitaxially grown film. We also study the effect of substrate pre-pattern amplitude on the film instability and island formation, and find the increase of island wave number (for maximum film instability) with the increasing substrate pattern amplitude.

APPENDIX A

Third order perturbation results of film elasticity

As described in Sec. 2.1, our perturbation approach developed here for solving the system elasticity problem can be extended to obtain higher order results through a recursive procedure. We have calculated the elastic properties of this heteroepitaxial system up to third order. In this appendix we present our results for the 3rd-order perturbed elastic energy density, which is given by

$$\begin{aligned}\tilde{\mathcal{E}}^{(3)f} &= \frac{E\epsilon}{1-\nu}\left[(1-\nu)\frac{a_1^{(3)}q_x + b_1^{(3)}q_y}{\mu q} - (1-2\nu)\frac{c_1^{(3)}}{2\mu}\right] \\ &+ \sum_{\mathbf{q}'}\left\{\frac{1+\nu}{2E}\left[\hat{\sigma}_{ij}^{(1)f}(\mathbf{q}')\hat{\sigma}_{ij}^{(2)f}(\mathbf{q}-\mathbf{q}') + \hat{\sigma}_{ij}^{(2)f}(\mathbf{q}')\hat{\sigma}_{ij}^{(1)f}(\mathbf{q}-\mathbf{q}')\right]\right. \\ &\left. -\frac{\nu}{2E}\left[\hat{\sigma}_{ll}^{(1)f}(\mathbf{q}')\hat{\sigma}_{ll}^{(2)f}(\mathbf{q}-\mathbf{q}') + \hat{\sigma}_{ll}^{(2)f}(\mathbf{q}')\hat{\sigma}_{ll}^{(1)f}(\mathbf{q}-\mathbf{q}')\right]\right\}, \qquad (1)\end{aligned}$$

where

$$a_1^{(3)} = \sum_{\mathbf{q}'}\left[(q_x - q_x')\hat{\sigma}_{xx}^{(2)f}(\mathbf{q}') + (q_y - q_y')\hat{\sigma}_{xy}^{(2)f}(\mathbf{q}')\right]\hat{h}(\mathbf{q}-\mathbf{q}'), \qquad (2)$$

$$b_1^{(3)} = \sum_{\mathbf{q}'}\left[(q_x - q_x')\hat{\sigma}_{xy}^{(2)f}(\mathbf{q}') + (q_y - q_y')\hat{\sigma}_{yy}^{(2)f}(\mathbf{q}')\right]\hat{h}(\mathbf{q}-\mathbf{q}'), \qquad (3)$$

$$c_1^{(3)} = \sum_{\mathbf{q}'} i\left[(q_x - q_x')\hat{\sigma}_{xz}^{(2)f}(\mathbf{q}') + (q_y - q_y')\hat{\sigma}_{yz}^{(2)f}(\mathbf{q}')\right]\hat{h}(\mathbf{q}-\mathbf{q}'). \qquad (4)$$

Based on the perturbation solutions of the system elasticity, we have obtained the first and second order results for the elastic stress tensor at film surface, which are used to calculate the perturbed elastic energy density given above. In second order we have

$$\begin{aligned}\hat{\sigma}_{xx}^{(2)f}(\mathbf{q}) &= -\frac{E\epsilon}{1-\nu}\sum_{\mathbf{q}'}\Bigg\{4\frac{q_x(q_x-q_x')}{q^3q'}(\nu q_y'^2+q_x'^2)(q^2+\nu q_y^2)\\ &+4\nu\frac{(q_y-q_y')q_y^3}{q^3q'}(q_y'^2+\nu q_x'^2)\\ &+4(1-\nu)\frac{q_x'q_y'}{q^3q'}\left[q_x(q_y-q_y')+q_y(q_x-q_x')\right](q_x^2+\nu q^2)\\ &-\frac{1}{q^2}\left[q_x'(q_x-q_x')+q_y'(q_y-q_y')\right](2\nu q_y^2+q_x^2)\\ &+4(1-\nu)\frac{q_xq_yq_x'q_y'}{q^3q'}\left[q_y(q_y-q_y')-q_x(q_x-q_x')\right]\Bigg\}\hat{h}(\mathbf{q}')\hat{h}(\mathbf{q}-\mathbf{q}'),\end{aligned}\tag{5}$$

$$\begin{aligned}\hat{\sigma}_{yy}^{(2)f}(\mathbf{q}) &= -\frac{E\epsilon}{1-\nu}\sum_{\mathbf{q}'}\Bigg\{4\frac{q_y(q_y-q_y')}{q^3q'}(\nu q_x'^2+q_y'^2)(q^2+\nu q_x^2)\\ &+4\nu\frac{(q_x-q_x')q_x^3}{q^3q'}(q_x'^2+\nu q_y'^2)\\ &+4(1-\nu)\frac{q_x'q_y'}{q^3q'}\left[q_x(q_y-q_y')+q_y(q_x-q_x')\right](q_y^2+\nu q^2)\\ &-\frac{1}{q^2}\left[q_x'(q_x-q_x')+q_y'(q_y-q_y')\right](2\nu q_x^2+q_y^2)\\ &-4(1-\nu)\frac{q_xq_yq_x'q_y'}{q^3q'}\left[q_y(q_y-q_y')-q_x(q_x-q_x')\right]\Bigg\}\hat{h}(\mathbf{q}')\hat{h}(\mathbf{q}-\mathbf{q}'),\end{aligned}\tag{6}$$

$$\hat{\sigma}_{zz}^{(2)f}(\mathbf{q}) = \frac{E\epsilon}{(1-\nu)}(3-2\nu)\sum_{\mathbf{q}'}\left[q_x'(q_x-q_x')+q_y'(q_y-q_y')\right]\hat{h}(\mathbf{q}')\hat{h}(\mathbf{q}-\mathbf{q}'),\tag{7}$$

$$\begin{aligned}\hat{\sigma}^{(2)f}_{xy}(\mathbf{q}) &= E\epsilon\sum_{\mathbf{q}'}\Big\{-4\frac{q_xq_y}{q'q^3}\left[\big(q_x(q_x-q'_x)(q'^2_x+\nu q'^2_y)+q_y(q_y-q'_y)(q'^2_y+\nu q'^2_x)\big)\right.\\ &+(1-\nu)q'_xq'_y\left(q_x(q_y-q'_y)+q_y(q_x-q'_x)\right)\Big]\\ &+\frac{(1-2\nu)}{(1-\nu)}\frac{q_xq_y}{q^2}\left[q'_x(q_x-q'_x)+q'_y(q_y-q'_y)\right]\\ &-\frac{4}{(1-\nu)}\frac{q_y^2}{q^3q'}\left[q_y(q_x-q'_x)(q'^2_x+\nu q'^2_y)-q_x(q_y-q'_y)(q'^2_y+\nu q'^2_x)\right.\\ &\left.+(1-\nu)q'_xq'_y\left(q_y(q_y-q'_y)-q_x(q_x-q'_x)\right)\right]\Big\}\hat{h}(\mathbf{q}')\hat{h}(\mathbf{q}-\mathbf{q}'),\end{aligned}\tag{8}$$

$$\begin{aligned}\hat{\sigma}^{(2)f}_{xz}(\mathbf{q}) &= \frac{2E\epsilon}{1-\nu}\sum_{\mathbf{q}'}i\frac{q_x}{q^2q'}\left\{q_x(q_x-q'_x)(q'^2_x+\nu q'^2_y)+q_y(q_y-q'_y)(q'^2_y+\nu q'^2_x)\right.\\ &+(1-\nu)q'_xq'_y\left[q_x(q_y-q'_y)+q_y(q_x-q'_x)\right]\\ &-\frac{q_y^2}{q_x}\left[(q_x-q'_x)(q'^2_x+\nu q'^2_y)+(1-\nu)(q_y-q'_y)q'_xq'_y\right]\\ &\left.+(1-\nu)q_y(q_x-q'_x)q'_xq'_y+q_y(q_y-q'_y)(q'^2_y+\nu q'^2_x)\right\}\hat{h}(\mathbf{q}')\hat{h}(\mathbf{q}-\mathbf{q}'),\end{aligned}\tag{9}$$

$$\begin{aligned}\hat{\sigma}^{(2)f}_{yz}(\mathbf{q}) &= \frac{2E\epsilon}{1-\nu}\sum_{\mathbf{q}'}i\frac{q_y}{q^2q'}\left\{q_x(q_x-q'_x)(q'^2_x+\nu q'^2_y)+q_y(q_y-q'_y)(q'^2_y+\nu q'^2_x)\right.\\ &+(1-\nu)q'_xq'_y\left[q_x(q_y-q'_y)+q_y(q_x-q'_x)\right]\\ &-\frac{q_x^2}{q_y}\left[(q_y-q'_y)(q'^2_y+\nu q'^2_x)+(1-\nu)(q_x-q'_x)q'_xq'_y\right]\\ &\left.+(1-\nu)q_x(q_y-q'_y)q'_xq'_y+q_x(q_x-q'_x)(q'^2_x+\nu q_y^2)\right\}\hat{h}(\mathbf{q}')\hat{h}(\mathbf{q}-\mathbf{q}'),\end{aligned}\tag{10}$$

while the results for first order perturbation are given by

$$\hat{\sigma}_{xx}^{(1)f}(\mathbf{q}) = \frac{2E\epsilon}{q(1-\nu)}(q_x^2 + \nu q_y^2)\hat{h}(\mathbf{q}), \tag{11}$$

$$\hat{\sigma}_{yy}^{(1)f}(\mathbf{q}) = \frac{2E\epsilon}{q(1-\nu)}(q_y^2 + \nu q_x^2)\hat{h}(\mathbf{q}), \tag{12}$$

$$\hat{\sigma}_{zz}^{(1)f}(\mathbf{q}) = 0, \tag{13}$$

$$\hat{\sigma}_{xy}^{(1)f}(\mathbf{q}) = 2E\epsilon\frac{q_x q_y}{q}\hat{h}(\mathbf{q}), \tag{14}$$

$$\hat{\sigma}_{xz}^{(1)f}(\mathbf{q}) = -\frac{E\epsilon}{1-\nu}iq_x\hat{h}(\mathbf{q}), \tag{15}$$

$$\hat{\sigma}_{yz}^{(1)f}(\mathbf{q}) = -\frac{E\epsilon}{1-\nu}iq_y\hat{h}(\mathbf{q}). \tag{16}$$

BIBLIOGRAPHY

[1] J. Stangl, V. Holy, and G. Bauer, "Structural properties of self-organized semiconductor nanostructures", Rev. Mod. Phys. **76**, 725 (2004).

[2] J. Tersoff et al, "Critical Island size for layer-by-layer growth", Phys. Rev. Lett. **72**, 266 (1994).

[3] M. Rost, P. Smilauer, and J. Krug, "Unstable epitaxy on vicinal surfaces", Surf. Sci. **369**, 393 (1996).

[4] I. Berbezier and A. Ronda, "SiGe nanostructures" ,Surf. Sci. Rep. **64**, 47 (2009).

[5] R. J. Asaro and W. A. Tiller, Metall. Trans. **3**, 1789 (1972),

[6] M. A. Grinfeld, Sov. Phys. Dokl. **31**, 831 (1986).

[7] S. Kiravittaya, A. Rastelli, and O. G. Schmidt, "Advanced quantum dot configurations", Rep. Prog. Phys. **72**, 046502 (2009).

[8] R. M. Tromp, F. M. Ross, and M. C. Reuter, "Instability-Driven SiGe Island Growth", Phys. Rev. Lett. **84**, 4641 (2000).

[9] J. Tersoff, B. J. Spencer, A. Rastelli, and H. von Känel, "Barrierless Formation and Faceting of SiGe Islands on Si(001)", Phys. Rev. Lett. **89**, 196104 (2002).

[10] D.E. Jesson and S.J. Pennycook, "Direct imaging of surface cusp evolution during strained-layer epitaxy and implications for strain relaxation", Phys. Rev. Lett. **71**, 1744 (1993).

[11] M.D. Seta, G. Capellini, F. Evangelisti, and C. Spinella, "Intermixing promoted Scaling of Ge/Si(100) island sizes", J. Appl. Phys. **92**, 614 (2002).

[12] R. C. Desai and R. Kapral, "Dynamics of Self-Organized and Self-Assembled Structures", (2009).

[13] Michael R. Mckay, John Shumway, and Jeff Drucker, "Real-time coarsening dynamics of Ge/Si(100) nanostructures", J. Appl. Phys. **99**, 094305 (2006).

[14] W. Dorsch et al, "Strain-induced island scaling during Si1xGex heteroepitaxy", Appl. Phys. Lett. **72**, 179 (1998).

[15] D. J. Srolovitz, Acta Metall. **37**, 621 (1989).

[16] B. J. Spencer, P. W. Voorhees, and S. H. Davis, "Morphological instability in epitaxially strained dislocation-free solid films", J. Appl. Phys. **73**, 4955 (1993).

[17] B. J. Spencer, P. W. Voorhees, and S. H. Davis, "Morphological instability in epitaxially strained dislocation-free solid films", Phys. Rev. Lett. **67**, 3696 (1991).

[18] P. Sutter and M. G. Lagally, "Nucleationless three dimensional island formation in low-misfit heteroepitaxy", Phys. Rev. Lett. **84**, 4637 (2000).

[19] J. E. Guyer and P. W. Voorhees, "Morphological Stability of Alloy Thin Films", Phys. Rev. Lett. **74**, 4031 (1995).

[20] B. J. Spencer, P. W. Voorhees, and J. Tersoff, "Morphological instability theory for strained alloy film growth: The effect of compositional stresses and species-dependent surface mobilities on ripple formation during epitaxial film deposition", Phys. Rev. B **64**, 235318 (2001).

[21] Z.-F. Huang and R. C. Desai, "Epitaxial growth in dislocation-free strained alloy films: Morphological and compositional instabilities", Phys. Rev. B **65**, 205419 (2002).

[22] Z.-F. Huang and R. C. Desai, "Instability and decomposition on the surface of strained alloy films", Phys. Rev. B **65**, 195421 (2002).

[23] R. C. Desai, H. K. Kim, A. Chatterji, D. Ngai, S. Chen, and N. Yang, "Epitaxial growth in dislocation-free strained asymmetric alloy films", Phys. Rev. B **81**, 235301 (2010).

[24] L. E. Shilkrot, D. J. Srolovitz, and J. Tersoff, "Morphology evolution during the growth of strained-layer superlattices", Phys. Rev. B **62**, 8397 (2000).

[25] L. E. Shilkrot, D. J. Srolovitz, and J. Tersoff, "Erratum: Morphology evolution during the growth of strained-layer superlattices", Phys. Rev. B **67**, 249901(E) (2003).

[26] Z.-F. Huang and R. C. Desai, "Stress-driven instability in growing multilayer films", Phys. Rev. B **67**, 075416 (2003).

[27] Z.-F. Huang, D. Kandel, and R. C. Desai, "Wetting effect and morphological stability in growth of short-period strained multilayers", Appl. Phys. Lett. **82**, 4705 (2003).

[28] F. M. Ross, J. Tersoff, and R. M. Tromp, "Coarsening of Self-Assembled Ge Quantum Dots on Si(001)", Phys. Rev. Lett. **80**, 984 (1998).

[29] A. Rastelli, M. Stoffel, J. Tersoff, G. S. Kar, and O. G. Schmidt, "Kinetic Evolution and Equilibrium Morphology of Strained Islands", Phys. Rev. Lett. **95**, 026103 (2005).

[30] J. A. Floro, M. B. Sinclair, E. Chason, L. B. Freund, R. D. Twesten, R. Q. Hwang, and G. A. Lucadamo, "Novel Sige Island Coarsening Kinetics: Ostwald Ripening and Elastic Interactions" Phys. Rev. Lett. **84**, 701 (2000).

[31] T. J. Krzyzewski and T. S. Jones, "Ripening and annealing effects in InAs/GaAs(001) quantum dot formation", J. Appl. Phys. **96**, 668 (2004).

[32] M. R. McKay, J. A. Venables, and J. Drucker, "Kinetically suppressed ostwald ripening of Ge/Si(100) hut clusters", Phys. Rev. Lett. **101**, 216104 (2008).

[33] G. Medeiros-Ribeiro, T. I. Kamins, D. A. A. Ohlberg, and R. S. Williams, "Annealing of Ge nanocrystals on Si(001) at 550 C: Metastability of huts and the stability of pyramids and domes", Phys. Rev. B **58**, 3533 (1998).

[34] W. Dorsch et al., "Strain-induced island scaling during Si1xGexheteroepitaxy", Appl. Phys. Lett. **72**, 179 (1998).

[35] J.L. Gray, R. Hull, and J.A. Floro, "Periodic arrays of epitaxial self-assembled SiGe quantum dot molecules grown on patterned Si substrates" J. Appl. Phys. **100** 084312 (2006).

[36] Takeshi Kitajima et al., "Two-dimensional periodic alignment of self-assembled Ge islands on patterned Si(001)surfaces" Appl. Phys. Lett. **80** 497 (2002).

[37] Zhenyang Zhong et al., "Ge island formation on stripe-patterned Si(001) substrates", Appl. Phys. Lett. **82**, 445 (2003).

[38] B. Sanduijav et al., "Shape transitions and island nucleation for Si/Ge molecular beam epitaxy on stripe-patterned Si (001) substrate", Phys. Rev. B **80**, 125329 (2009).

[39] Zhenyang Zhong et al., "Positioning of self-assembled Ge islands on stripe-patterned Si(001) substrates" J. Appl. Phys. **93** 6258 (2003).

[40] T. Ishikawa et al., "site control if InAs quantum dots on GaAs surfaces patterend ny in situ electron-beam lithography" J. Vac. Sci. Technol. B **18** 2635 (2000).

[41] W. Ye et al., "Control of InAs/GaAs quantum dot density and alignment using modified buffer layers" J. Vac. Sci. Technol. B **23** 1736 (2005).

[42] G. Nandipati and J. G. Amar, "Effects of strain on island morphology and size distribution in irreversible submonolayer growth", Phys. Rev. B **73**, 045409 (2006).

[43] T. P. Schulze and P. Smereka, "An energy localization principle and its application to fast kinetic Monte Carlo simulation of heteroepitaxial growth", J. Mech. Phys. Solids **57**, 521 (2009).

[44] K. R. Elder, M. Katakowski, M. Haataja, and M. Grant, "Modeling Elasticity in crystal growth", Phys. Rev. Lett. **88**, 245701 (2002).

[45] Z.-F. Huang and K. R. Elder, "Mesoscopic and microscopic modeling of island formation in strained film epitaxy", Phys. Rev. Lett. **101**, 158701 (2008).

[46] Z.-F. Huang and K. R. Elder, "Morphological instability, evolution, and scaling in strained epitaxial films: An amplitude-equation analysis of the phase-field-crystal model", Phys. Rev. B **81**, 165421 (2010).

[47] K.-A. Wu and P. W. Voorhees, "Stress-Induced Morphological Instabilities at the Nanoscale Examined Using the Phase Field Crystal Approach" Phys. Rev. B **80**, 125408 (2009).

[48] K. R. Elder, Z.-F. Huang, and N. Provatas, "Amplitude expansion of the binary phase-field-crystal model", Phys. Rev. E **81**, 011602 (2010).

[49] K. R. Elder and Z.-F. Huang, "A phase field crystal study of epitaxial island formation on nanomembranes", J. Phys.: Condens. Matter **22**, 364103 (2010).

[50] Z.-F. Huang, K. R. Elder, and N. Provatas, "Phase-field-crystal dynamics for binary systems: Derivation from dynamical density functional theory, amplitude equation

formalism, and applications to alloy heterostructures", Phys. Rev. E **82**, 021605 (2010).

[51] W. H. Yang and D. J. Srolovitz, "Cracklike surface instabilities in stressed solids", Phys. Rev. Lett. **71**, 1593 (1993).

[52] B. J. Spencer, S. H. Davis, and P. W. Voorhees, "Morphological instability in epitaxially strained dislocation-free solid films: Nonlinear evolution", Phys. Rev. B **47**, 9760 (1993).

[53] C.-h. Chiu, "The self-assembly of uniform heteroepitaxial islands", Appl. Phys. Lett. **75**, 3473 (1999).

[54] C.-H. Chiu and Z. Huang, "Numerical simulation for the formation of nanostructures on the StranskiKrastanow systems by surface undulation", J. Appl. Phys. **101**, 113540 (2007).

[55] F. Liu, A. H. Li, and M. G. Lagally, "Self-Assembly of Two-Dimensional Islands Via Strain-Mediated Coarsening", Phys. Rev. Lett. **87**, 126103 (2001).

[56] Y. Xiang and E. Weinan, "Nonlinear evolution equation for the stress-driven morphological instability" J. Appl. Phys. **91**, 9414 (2002).

[57] P. Liu, Y. W. Zhang, and C. Lu, "Coarsening kinetics of heteroepitaxial islands in nucleationless Stranski-Krastanov growth" Phys. Rev. B **68**, 035402 (2003).

[58] A. A. Golovin, S. H. Davis, and P. W. Voorhees, "Self-Organization of Quantum Dots in Epitaxially-Strained Solid Films", Phys. Rev. E **68**, 056203 (2003).

[59] W. T. Tekalign and B. J. Spencer, "Evolution equation for a thin epitaxial film on a deformable substrate", J. Appl. Phys. **96**, 5505 (2004).

[60] W. T. Tekalign and B. J. Spencer, "Thin-film evolution equation for a strained solid film on a deformable substrate: Numerical steady states" J. Appl. Phys. **102**, 073503 (2007).

[61] H. R. Eisenberg and D. Kandel, "Formation, ripening, and stability of epitaxially strained island arrays", Phys. Rev. B, **71**, 115423 (2005).

[62] Y. Pang and R. Huang, "Nonlinear effect of stress and wetting on surface evolution of epitaxial thin films" Phys. Rev. B **74**, 075413 (2006).

[63] M. S. Levine, A. A. Golovin, S. H. Davis, and P. W. Voorhees, "Self-Assembly of Quantum Dots in a Thin Epitaxial Film Wetting an Elastic Substrate", Phys. Rev. B **75**, 205312 (2007).

[64] J.-N. Aqua, T. Frisch, and A. Verga, "Nonlinear evolution of a morphological instability in a strained epitaxial film", Phys. Rev. B **76**, 165319 (2007).

[65] J. Muller and M. Grant, "Model of Surface Instabilities Induced by Stress", Phys. Rev. Lett. **82**, 1736 (1999).

[66] K. Kassner, C. Misbah, J. Müller, J. Kappey, and P. Kohlert, "Phase-field modeling of stress-induced instabilities", Phys. Rev. E **63**, 036117 (2001).

[67] J.-N. Aqua, T. Frisch, and A. Verga, "Ordering of strained islands during surface growth", Phys. Rev. E **81**, 021605 (2010).

[68] M. C. Cross, D. I. Meiron, and Y. Tu, "Chaotic domains: a numerical investigation", Chaos **4**, 607 (1994).

[69] B. J. Spencer and D. I. Meiron, Acta Metall. Mater. **37**, 621 (1994)

[70] F. M. Ross, J. Tersoff, and R. M. Tromp, "Coarsening of Self-Assembled Ge Quantum Dots on Si(001)", Phys. Rev. Lett. **80**, 984 (1998).

[71] C. Sagui and R. C. Desai, "Kinetics of phase separation in two-dimensional systems with competing interactions", Phys. Rev. E, **49**, 2225 (1994).

ABSTRACT

CONTINUUM ELASTICITY MODELING OF NANOSTRUCTURE EVOLUTION IN STRAINED FILM EPITAXY

by

CHAMPIKA G GAMAGE

December 2012

Advisor: Dr. Zhi-Feng Huang

Major: Physics

Degree: Doctor of Philosophy

The formation of surface nanostructures such as islands or quantum dots during strained film epitaxy has attracted great interest in recent years. The underlying mechanisms have been attributed to the occurrence of morphological instabilities of the strained films, for which the coupling between film-substrate material properties and growth conditions plays a major role. Morphological properties of an epitaxially grown film and the self-organization process of coherent strained islands are analyzed via the development of a continuum elasticity model based on the 2nd order perturbation method. Effects of wetting stress due to film-substrate interactions have been incorporated in the resulting nonlinear dynamic equation governing the film morphological profile. We study the formation and evolution of surface strained islands or quantum dots for different film/substrate misfit strains, via analyzing the time-dependent behavior of the structure factor for surface heights, its various moments, and the surface roughness. Three regimes of island array evolution have been identified, including a film instability regime at early stage, a slow power-law-type coarsening at intermediate time, and the crossover to a sat-

urated state, with detailed behavior dependent on misfit strains but not qualitatively on finite system sizes. It is found to be controlled by the strength of film-substrate wetting interaction which would constrain the valley-to-peak mass transport and hence the growth of island height, and also determined by the effect of elastic interaction between surface islands and the high-order strain energy of individual islands at late evolution stage. The results are compared to previous experimental and theoretical efforts on quantum dots coarsening and saturation. We also study the formation of these nanostructures on a nonplanar patterned substrate. The properties of islands formed are highly affected and controlled by the periodicity and amplitude of the pre-defined substrate patterns and also the initial film thickness, as shown in our stability analysis results.

AUTOBIOGRAPHICAL STATEMENT

CHAMPIKA G GAMAGE

EDUCATIONAL QUALIFICATIONS

Ph.D. Candidate in Physics, Wayne State University, Detroit
MS in Physics, Wayne State University, Detroit, 2009
BS in Physics, University of Colombo, Sri Lanka, 2004

PROFESSIONAL EXPERIENCE

Graduate Research Assistant, Wayne State University, 2008 May to 2012
Graduate Teaching Assistant, Wayne State University, 2006 August to 2008 April
College teacher in Mathematics, Royal Institute, Sri Lanka, 2005 to 2006
Instructor in Physics, University of Colombo, Sri Lanka, 2004

AWARDS, AFFILIATIONS & ACTIVITIES

Member of the main organizing committee of the graduate research exhibition 2012, Department of Physics and Astronomy, Wayne State University
Daniel R. Gustafson Graduate Student Teaching Award, Wayne State University 2008
Student member of American Physical Society

PUBLICATIONS AND PRESENTATIONS

Nonlinear dynamics of island coarsening and stabilization during strained film heteroepitaxy, Champika G Gamage and Zhi-Feng Huang, submitted to Physics Review E, 2012
Strained Islands Evolution during Thin Film Heteroepitaxy with Planar and Pre-patterned Substrates, Ohio-Region Section Meeting of the American Physical Society, Detroit, Michigan, 2012 (Oral Talk)
Coarsening and saturation of quantum dot evolution during strained film heteroepitaxy, American Physical Society March Meeting, Dallas, Texas 2011 (Oral Talk)
Strained quantum dot evolution during thin film heteroepitaxy, Wayne State University, Second Annual Graduate Exhibition, 2011 (Poster)
Continuum elasticity modeling and nonlinear effects during epitaxially strained island evolution, Ohio-Region Section Meeting of the American Physical Society, Flint, Michigan, 2010 (Poster)
Continuum elasticity modeling and nonlinear effects during epitaxially strained island evolution, Department of Physics and Astronomy, Wayne State University, Graduate Research Day, 2010 (Poster)
Continuum elasticity modeling and nonlinear effects during epitaxially strained island evolution, American Physical Society March Meeting, Portland, Oregon 2010 (Oral Talk)